






Article

A Study on a Compact Double Layer Sub-GHz Reflectarray Design Suitable for Wireless Power Transfer

Romans Kuskins ^{*}, Darja Cirjulina , Janis Eidaks , Kristaps Gailis, Ruslans Babajans , Anna Litvinenko , Deniss Kolosovs  and Dmitrijs Pikulins 

Institute of Photonics, Electronics and Telecommunications, Riga Technical University, 12 Azenes Street, LV-1048 Riga, Latvia; darja.cirjulina@rtu.lv (D.C.); janis.eidaks@rtu.lv (J.E.); kristaps.gailis@rtu.lv (K.G.); ruslans.babajans@rtu.lv (R.B.); anna.litvinenko@rtu.lv (A.L.); deniss.kolosovs@rtu.lv (D.K.); dmitrijs.pikulins@rtu.lv (D.P.)

* Correspondence: romans.kuskins@rtu.lv

Abstract: The paper presents a novel small-footprint varactor diode-based reconfigurable reflectarray (RRA) design and investigates its power reflection efficiency theoretically and experimentally in a real-life indoor environment. The surface is designed to operate at 865.5 MHz and is intended for simultaneous use with other wireless power transfer (WPT) efficiency-improving techniques that have been recently reported in the literature. To the best of the authors' knowledge, no RRA intended to improve the performance of antenna-based WPT systems operating in the sub-GHz range has been designed and studied both theoretically and experimentally so far. The proposed RRA is a two-layer structure. The top layer contains electronically tunable phase shifters for the local phase control of an incoming electromagnetic wave, while the other one is fully covered by metal to reduce the phase shifter size and RRA's backscattering. Each phase shifter is a pair of diode-loaded 8-shaped metallic patches. Extensive numerical studies are conducted to ascertain a suitable set of RRA unit cell parameters that ensure both adequate phase agility and reflection uniformity for a given varactor parameter. The RRA design parameter finding procedure followed in this paper comprises several steps. First, the phase and amplitude responses of a virtual infinite double periodic RRA are computed using full-wave solver Ansys HFSS. Once the design parameters are found for a given set of physical constraints, the phase curve of the corresponding finite array is retrieved to estimate the side lobe level due to the finiteness of the RRA aperture. Then, a diode reactance combination is found for several different RRA reflection angles, and the corresponding RRA radiation pattern is computed. The numerical results show that the side lobe level and the deviation of the peak reflected power angles from the desired ones are more sensitive to the reflection coefficient magnitude uniformity than to the phase agility. Furthermore, it is found that for scanning angles less than 50°, satisfactory reflection efficiency can be achieved by using the classical reactance profile synthesis approach employing the generalized geometrical optics (GGO) approximation, which is in accord with the findings of other studies. Additionally, for large reflection angles, an alternative synthesis approach relying on the Floquet mode amplitude optimization is utilized to verify the maximum achievable efficiency of the proposed RRA at large angles. A prototype consisting of 36 elements is fabricated and measured to verify the proposed reflectarray design experimentally. The initial diode voltage combination is found by applying the GGO-based phase profile synthesis method to the experimentally obtained phase curve. Then, the voltage combination is optimized in real time based on power measurement. Finally, the radiation pattern of the prototype is acquired using a pair of identical 4-director printed Yagi antennas with a gain of 9.17 dBi and compared with the simulated. The calculated results are consistent with the measured ones. However, some discrepancies attributed to the adverse effects of biasing lines are observed.

Keywords: compact reflectarray; wireless power transfer; sub-gigahertz band; double layered reflector



Citation: Kuskins, R.; Cirjulina, D.; Eidaks, J.; Gailis, K.; Babajans, R.; Litvinenko, A.; Kolosovs, D.; Pikulins, D. A Study on a Compact Double Layer Sub-GHz Reflectarray Design Suitable for Wireless Power Transfer. *Electronics* **2024**, *13*, 2754. <https://doi.org/10.3390/electronics13142754>

Academic Editor: Fabio Corti

Received: 12 June 2024

Revised: 4 July 2024

Accepted: 10 July 2024

Published: 13 July 2024



Copyright: © 2024 by the authors. Licensee MDPI, Basel, Switzerland. This article is an open access article distributed under the terms and conditions of the Creative Commons Attribution (CC BY) license (<https://creativecommons.org/licenses/by/4.0/>).

1. Introduction

Next-generation wireless communication systems, such as 6G, as well as emerging technologies, including the Internet of Things (IoT), face numerous challenges hampering their rapid development. While self-propelled vehicles and robots can easily maintain data exchange with other devices or base stations wirelessly, the battery charging process is still not imaginable without cords. In some cases, the lack of efficient wireless charging capabilities may be highly inconvenient (e.g., sensor nodes incorporated in various building structure elements to perform their structural health monitoring, in particular, ancient buildings, temples, and castles) or even life-threatening (e.g., in various medical applications).

The existing wireless power transfer (WPT) techniques demonstrate sufficiently high power transfer efficiency only under certain conditions. For example, inductive wireless power transfer systems are capable of maintaining reasonable WPT efficiency only over small distances between the transmitting and the receiving coil compared with the coil dimensions. The reason is that the mutual coupling between the coils weakens rapidly with increasing intercoil separation. While the resonant cavity-enabled WPT systems have been shown to ensure high WPT efficiency over large volumes of space, they, however, require metallic enclosure and are typically highly sensitive to the position of metallic objects in the interior of the cavity and wall conduction losses. Furthermore, due to high conductivity, the cavity walls reduce or entirely inhibit any wireless communication with the exterior of such a cavity. This poses a significant inconvenience for numerous indoor settings, like office spaces, where maintaining stable wireless data connections is crucial.

As regards the farfield antenna-based WPT systems, their main drawback is significant path loss, which increases very quickly with the operating frequency. On the other hand, transferring power by means of antennas at lower frequencies cannot guarantee high WPT efficiency, either, due to low RF-DC converter efficiencies at low frequencies.

The path-loss issue in antenna-based WPT systems could be addressed by deploying a reflectarray (RA)-based real-time reconfigurable power transfer environment capable of adapting the power transfer channel to increase the amount of power received by an intended receiver. Furthermore, in recent years, reconfigurable RAs (RRAs) have been extensively studied in connection with another emerging application, namely, Intelligent Reflecting Surface (IRS)-assisted communication links [1]. Deploying reconfigurable propagation environments has recently demonstrated the ability to substantially improve communication channel characteristics in enclosed environments such as office rooms and various industrial facilities [2].

While ongoing research in the field of RRAs is mostly focused on developing the Intelligent Reconfigurable Surface (IRS) concept, it is possible to leverage RRA's power to enhance the power transfer efficiency of antenna-based WPT systems deployed in indoor environments [3,4]. For adaptable antenna-based WPT systems to guarantee reasonable power transfer efficiency while being affordable and cost-effective, the RRAs must be low-loss, easy to adjust, and, more importantly, inexpensive. This fact motivated the present study, which is aimed at developing an efficient, easy-to-manufacture, and low-cost RRA design intended to steer the power beam in the desired direction.

The concept of RAs was originally developed by Berry and described in his seminal paper [5]. The first RA proposed in [5] employed short-circuited waveguide sections to eliminate the phase errors across the surface of a planar structure to attain a collimated pencil beam in the desired direction. Despite possessing numerous beneficial and appealing features, such as being lightweight and compact, having a low-profile design, being easy to manufacture, and being highly efficient, RAs did not gain popularity within the microwave community until the early 90s, coinciding with the onset of significant advancements in the field [6].

Other early incarnations of this concept employed metallic patches of variable sizes to achieve a desired reflection coefficient phase variation across the RA surface [7,8]. Later, designs involving more complicated phase-shifter (surface resonator) shapes were proposed

to improve the performance of static RAs [9]. Realizing an appropriate phase profile generates a wave propagating in a required direction (at a specific angle). Such simple RAs have been found to be useful in static antenna configurations where the direction of the wave illuminating the RA is invariant [10,11]. Specifically, the RAs are employed as reflectors intended to collimate a spherical electromagnetic wave radiated by a feed antenna (e.g., a horn antenna) into a pencil beam steered in a specific direction.

While in many practical cases (e.g., static pencil beam antennas), fixed RA configurations are sufficient to ensure sufficient wave power conversion efficiencies, some applications, including emerging ones, might significantly benefit from the use of reconfigurable RAs (RRAs) [12]. In contrast to classical static configuration designs, the phase profile across the surface can be altered by changing the position or properties of the phase shifters in the RRA. Thus, RRAs are more flexible, as their phase patterns can be altered in real time, enabling beam scanning performance. For this reason, the microwave community's efforts have been focused on developing low-loss reconfigurable RAs (RRA). RRAs can potentially address the increased demand for stable communication links within indoor environments where the adverse effects of diffraction and multi-path propagation may lead to a drastic degradation of communication quality [13].

Mechanically reconfigurable RAs have been shown to guarantee sufficiently high gain characteristics [14]. Nonetheless, dynamically changing the phase profile enables adaptable reflection systems to demonstrate higher scan speed, which is more advantageous for many beam-scanning applications. An alternative approach to implementing reconfigurable structures relies on integrating metallic reflectarray phase shifters with lumped elements whose parameters can be changed in real time by applying different voltage levels [15–17].

More elaborate designs leveraging recent advances in material science might potentially improve RA efficiency, especially in high-frequency systems where semiconductor phase shifter losses become more pronounced. For instance, using liquid crystal-based RAs allows the phase profile to be adjusted by altering the unit cells' effective dielectric constant individually by applying different voltage levels across them [18]. Some recent studies demonstrated the possibility of realizing a thermally actuated vanadium dioxide-based RA highly suitable for millimeter-wave range applications [19,20]. RA antennas based on ferroelectric thin-film [21] and novel photonically controlled [22] phase shifters have been shown to exhibit low losses compared to their diode-based counterparts. Advanced materials with remarkable properties, such as graphene, have also been found to be useful in RA technology. Graphene-based RAs are well suited for terahertz applications where reasonable efficiency is tremendously hard to maintain due to excessively high losses [23].

Micro-electromechanical systems allow for achieving different phase profiles via altering RRA phase shifter geometry, similar to purely mechanical RRAs [24]. As a result, RRAs incorporating MEMS tend to have much lower insertion loss than varactor diode-based RRAs. Furthermore, they are typically less expensive due to their simpler fabrication, low power consumption, and compactness. The most prominent disadvantages of MEMS-based RRAs are low speed and mechanical reliability [25].

Regarding the RA performance over a wide frequency band, the following two factors considerably limit the bandwidth. The first factor is the inherently narrow bandwidth of microstrip elements due to their resonant nature. Consequently, the half-wavelength element-based RAs, and to a lesser extent, their sub-wavelength counterparts, exhibit appreciable reflection phase variations with the working frequency. Therefore, the RA bandwidth is typically severely limited to about 3% or so. Efforts focused on improving RA bandwidth have given rise to various attractive wideband and multi-band designs [26]. The other RA bandwidth limiting factor is the non-uniform variation of path lengths between the feed and the reflector with frequency [27].

The simplest techniques to extend the reflecting antenna bandwidth include employing thicker substrates, several coupled resonant elements, and constructing multilayered structures by stacking a few metallic patches or resonators with other shapes [28]. The use of sequentially rotated element groups has also been shown to increase the RA bandwidth

by up to 15%. The effect of the frequency-dependent phase shifts due to variation of electrical distance between the surface elements and the feed can be reduced by employing the so-called True-Time Delay (TTD) elements [29]. RA antennas constructed from subwavelength patch elements are less resonant than the half-wavelength patches and, therefore, demonstrate an acceptably small performance variation over wider frequency bands [30–32]. An additively manufactured metal-only design demonstrating wideband achromatic performance is treated in [33].

Typically, conventional electronically tunable RA designs tend to show significantly narrower usable bands in which the phase agility stays within acceptable limits. The reason is that most tunable phase shifter-based arrangements use simple resonators with well-separated resonant frequencies, which ensure bandwidth on the order of 1–2% [34]. While it is possible to improve bandwidth by means of multi-layered structures, single-layered structures are preferred in practice due to their lower cost and ease of fabrication. The first single-layer multi-resonant (double resonant) RA design composed of two coplanar split rings loaded by varactor diodes was proposed in [34]. Owing to greater phase agility, this design was shown to achieve 2.4% bandwidth at 5.4 GHz. These results inspired several other studies aimed at further improving the bandwidth via the use of more sophisticated reconfigurable designs [35,36], including wideband antenna containing metal phase shifters to ensure high power handling capacity reaching 4.5 GW/m^2 for a deflection angle span up to 120° [37,38] suitable for high-power microwave applications. Strong coupling between adjacent elements due to close spacing between printed dipoles is another viable approach to extending RA bandwidths [39]. In [40], a simple wideband discrete phase state PIN diode-based RA array with 1-bit resolution and a bandwidth of 8.4% at 5.0 GHz is proposed and studied.

Circularly polarized (CP) waves are also extensively used in wireless communication owing to their reduced susceptibility to certain types of interference. Thus, over the last few decades, a number of RRA designs capable of handling CP waves in an efficient manner have been developed [41,42]. Since some applications exploit polarization diversity to mitigate various propagation channel imperfections, more elaborate RRA designs enabling individual manipulation of different linear [43,44] or circularly polarization states [45,46] have also been proposed.

Depending on the local phase control type, the electronically tunable RRAs fall into one of the following two categories: (1) continuously tunable phase shifters; (2) discrete ones. The latter, typically, offer simpler dynamic reconfiguration at the expense of increased side lobe level. However, in many cases, the efficiency reduction is modest, even for configurations composed of two-phase state elements (1-bit phase resolution) [47,48], provided proper optimization is performed. The discrete phase reconfigurable surfaces can also handle two linearly polarized waves independently [49]. Additionally, several switchable 1-bit reflecting surface designs capable of manipulating two circularly polarized waves of opposite senses independently from one another have been proposed and examined in recent years [50,51]. A comprehensive study of the angular and polarisation stability of 1-bit RAs was carried out in [52]. The miniaturization of discrete phase RA designs and a reduction in the number of PIN diodes have also been recently attempted [53,54]. A downside of the tunable resonator-based RA topologies is rather intricate biasing networks and more complicated control commands. Despite this, at millimeter frequencies, where varactor diodes can no longer be used due to prohibitively high losses, discrete RRAs may be more attractive from both the manufacturing and efficiency point of view than RRAs employing advanced tunable materials [55].

It is noteworthy that few studies have demonstrated a possibility of mitigating the effect of RA element misalignment, which is a serious issue. A malleable membrane-based reflector is used in [56], allowing for appreciable weight and volume reductions, which is of utmost importance in various space applications, as described [57].

The present paper is organized as follows. Section 1 briefly reviews the history, applications, and operating principles of reconfigurable RAs. Section 2 explains the choice of the

passive beamforming strategy and describes various technical aspects and considerations of reflectarrays designs. Section 3 Presents the Ansys HFSS models for infinite periodic planar reflecting surfaces constructed to find the most suitable RRA unit cell parameters and verify the applicability of the chosen unit cell topology. Additionally, simulation results are presented for both the infinite RA model and the finite ones. Section 4 describes the fabricated RA prototype and the experimental real-time measurement-based optimization procedure developed to improve the RA efficiency for different desired reflection angles. Also, the section discusses the measurement results obtained for an experimental setup involving the RA prototype and two printed Yagi antennas. The final section concludes the paper.

2. Materials and Methods

Establishing a LoS preparation channel in indoor environments is, in many cases, quite problematic due to many obstacles, such as various furniture elements (in office rooms) or dedicated equipment (in the case of industrial facilities) blocking the signal propagation path. Consequently, a power-carrying signal undergoes multiple reflections off the room walls and various objects. With each reflection, its intensity decreases, potentially requiring a higher power level for the signal reaching the intended receiver. Though strong scattering due to diffraction on knife-edge discontinuities and multipath propagation may ensure an acceptable amount of power arriving at the receiver, it is difficult to control. The RRA's capability to focus and redirect the power of an incoming wave toward a direction may increase WPT efficiency by altering the power transfer channel.

This property of the RRA may enable stable wireless communications even when there is no LoS propagation between a power transmitter and an intended receiver, which is often the case when data transmission is performed in indoor environments with complex geometry, such as the L-shaped corridor depicted in Figure 1.

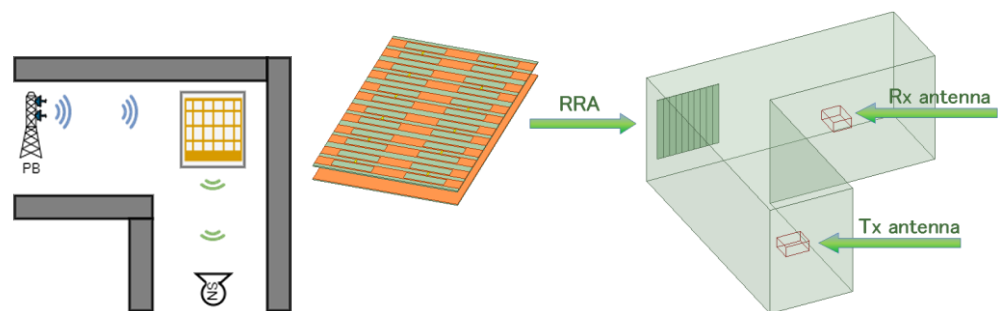


Figure 1. An illustration of an RRA-enhanced WPT system in an indoor environment. PB and SN stand for a power beacon and a sensor node, respectively.

2.1. Choice of the RRA Topology

The use of specially designed reflectors capable of redirecting incoming power-carrying waves toward the receiving antenna or other reflectors may address the fading due to multipath propagation and strong scattering by various objects present in an indoor environment, thereby considerably improving the overall efficiency of antenna-based WPT system deployed therein. The simplest solution would be to place reflectors at various positions in the environment. Some recent studies demonstrated the possibility of improving the WPT system's efficiency through the use of RAs [58,59]. However, these RAs are not reconfigurable, which limits their use to situations where the power transmitter and the intended receiver have fixed positions. Alternatively, this approach to increasing the RX power is not suitable for dynamic WPT systems, where either the receiver or transmitter, or, in general, both can move freely across the environment. Of course, situations where only the receiver is movable are more common in practice, e.g., in some mobile home appliances or robots. To enhance WPT efficiency in dynamic environments, there is a need for more

flexible reflector-based systems capable of dynamically altering a power transfer channel in real-time.

Mechanically tunable reflectors can address the above issue. For example, the use of parabolic reflectors equipped with motors and other mechanics makes it possible to shift and rotate the reflector to form a narrow beam toward the receiving antenna. A severe downside of this approach is that the transverse dimensions of the reflecting surface must be much larger compared to a wavelength at the working frequency to achieve high gain. Accordingly, such reflectors are too large at low frequencies to seamlessly integrate into small- or medium-size indoor environments.

RRAs are a viable alternative to the bulky mechanically tunable reflectors, such as the one reported in [60]. Antenna-based RRAs resemble phased array antennas (PAA) in that they also incorporate multiple periodically arranged planar antennas (e.g., microstrip patch or dipole antennas) but require no generators, enabling efficient passive beamforming. Classical half-wavelength antenna-based reflectarrays are highly attractive from the theoretical analysis perspective owing to weak inter-element coupling. This allows for treating them using the existing well-developed methods for antenna array analysis, which are not computationally demanding. However, due to their resonant nature, the antenna-based RRAs demonstrate adequate behavior only over a limited frequency band.

The advent of metasurfaces shifted the focus of RA researchers toward designs involving subwavelength elements, which proved to be not only a good substitute for an antenna-based RA but also an effective means to remedy the limited bandwidth problem. Transforming impedance surfaces into tunable ones is straightforward through the integration of variable capacitance elements. The most suitable candidate for the variable capacitor is varactor diodes.

2.2. Design Considerations

The operating frequency must adhere to regulations governing the frequency spectrum, which restrict the transmission of information and power transfer via electromagnetic waves to specific bands. Another essential factor to consider when designing RRA is the efficiency of the RF-DC converter used on the receiving side to convert the received high-frequency signal into a DC voltage needed to power the sensor node circuitry directly or to accomplish battery charging. Increasing the operating frequency requires more expensive diodes to ensure adequate power conversion efficiency (PCE) and reduce the WPT range due to higher path-loss.

The operating frequency for the RRA under study is 865.5 MHz—the choice dictated by several considerations. First, this frequency belongs to one of the ISM bands (open for scientific use). Second, at this frequency, the path loss remains manageable, ensuring that power transfer across a medium-sized indoor environment is not significantly compromised.

Other factors to be considered when constructing an effective RRA are the power reflection efficiency of the RRA and its size. On the one hand, for small or medium-sized indoor environments, small outline RRAs are preferable since the environmental dimensions impose tight constraints on the RRA size. The presence of furniture further tightens the constraints. On the other hand, RRAs with smaller dimension-to-wavelength ratios exhibit considerably higher side lobe levels, reducing the amount of power sent in the desired direction. However, as will be shown in what follows, using three PCB panels (the width of a single panel is 30 cm) yields sufficiently high reflected power for the reflection angles up to 50°.

The distance between the transmitting antenna and the RRA panels must also be taken into consideration when choosing a suitable RRA design. For large RRA panels, the distance between the transmitting antenna and the RRA must be large for the plane wave approximation to hold; otherwise, RRA performance will be degraded. Although this issue can be mitigated owing to the capability of RRA to transform a spherical wave into a pencil beam, this approach necessitates a large codebook (a set of phase profiles) that may be impractical or even unachievable by some RRA designs.

2.3. Analysis of the Subwavelength Reconfigurable Reflectarray

In this paper, the structure under study is treated numerically using the general-purpose numerical method, namely, the finite element method. The RRA phase profile is extracted from the phase curve calculated for a numerical RRA model [61,62]. The relation between the incident plane wave and the reflected one is assumed to follow the principles of the generalized geometrical optics approximation-based approach. Specifically, the surface is assumed to be infinite in extent and composed of elements (phase shifters) of infinitesimal dimensions for the calculation of a continuous phase profile. Then, the synthesized profile is discretized to make it realizable with real-life finite subwavelength resonators acting as phase shifters.

Although the availability of closed-form expressions for the required phase profile makes the GGO-based synthesis method highly convenient, it is plagued by severe limitations. The comprehensive examination of the realizability of the RA can be found in [63], where it is proved that perfect incident plane wave conversion into a single unmodulated plane wave propagating away from the surface is not achievable with lossless RA. The reason is that the normal component of the Poynting vector on the surface of the RA is spatially dispersive, exhibiting oscillations along the surface. The oscillations vanish only when the reflection angle is equal to the angle of incidence (specular reflection) or is the negative of it (retroreflection). However, both cases are of little practical interest. As a result, the use of passive lossless reflecting surfaces inevitably results in oscillations in the amplitude of the reflected wave (modulation) in cases other than those mentioned before, which yields a spatial dependence that differs considerably from the desired one.

One way to eliminate this spatial variation is to consider lossy RAs [63], but the wave conversion efficiency deteriorates substantially as the deflection angle increases. In the limiting case, as the reflection angle approaches 90°, the reflected power tends to zero due to strong power absorption, thus making the RAs designed in this way highly impractical. This fact considerably limits the applicability of the sub-wavelength element-based RRA, as one can achieve reasonable wave conversion efficiency only for small angles. However, the theoretical and experimental studies demonstrate that this limitation is less severe than it might seem at first glance. A more in-depth treatment of this issue will be provided in our forthcoming papers. For small deflection angles, the generalized optics-based synthesis procedure can provide reasonably good efficiency. For larger angles, however, more sophisticated RRA synthesis means should be used.

The electric field of the incident plane wave with the amplitude $E_{x,0}^i$ is given by

$$E_x^i(x, z) = E_{x,0}^i e^{-jk_x x} e^{jk_z z} = E_{x,0}^i e^{-jk_0 \sin \theta^i x} e^{jk_0 \cos \theta^i z}, \tag{1}$$

where k_0 is the free space wavenumber, θ^i is the angle of incidence, θ^r is the desired reflection angle, $\varphi(x)$ is the required phase profile to achieve a reflected plane wave propagating away from the RRA at an angle of θ^r , x is the coordinate in the azimuthal plane of the RRA, and $\lambda_0 = c/f$ is the wavelength at the operating frequency, f .

The main purpose of the RRA is to produce the following reflected wave

$$E_x^r(x, z) = E_{x,0}^r e^{-jk_0 \sin \theta^r x} e^{-jk_0 \cos \theta^r z} = r(x) \cdot E_{x,0}^i e^{-jk_0 \sin \theta^i x} e^{-jk_0 \cos \theta^r z}, \tag{2}$$

where the local reflection coefficient is defined as $r(x) = R_0 e^{jk_0(\varphi_0 + x \sin \theta^i - x \sin \theta^r)}$, φ_0 is an arbitrary coordinate invariant phase term, $\cos \theta^r = \sqrt{1 - \sin^2 \theta^r}$, $E_{x,0}^r$ is the amplitude of the reflected plane wave, and R_0 is the magnitude of the reflection coefficient.

To achieve this, the RRA must have a non-uniform response to the incident wave. Alternatively, the relation between the electric field intensity of the incident and the reflected waves at the RRA surface must be of the form.

$$\frac{2\pi}{\lambda_0} (\sin \theta^i - \sin \theta^r) = \frac{d\varphi(x)}{dx}, \tag{3}$$

where $\varphi(x)$ is the desired phase profile of the RRA.

Integrating (3) gives the following expression for the RA reflection phase profile required to launch the reflected plane wave toward θ^r

$$\varphi_0 + 2\pi/\lambda_0(\sin\theta^i - \sin\theta^r)x = \varphi(x), \quad (4)$$

The perfect linear phase profile given by (4) ensures proper functioning of the RA but, unfortunately, cannot be realized by periodic arrangements of sub-wavelength phase shifters; the optimal approach is to realize a staircase approximation of the desired phase profile. In general, the phase profile discretization gives rise to spurious lobes in the RA radiation pattern, which may lead to appreciable power leakage in unwanted directions. In some cases, this additional loss source may dramatically degrade the overall WPT system efficiency. At first glance, this problem can be mitigated by building RA designs with smaller resonators—the smaller the size compared to a wavelength, the better. However, the authors' numerical studies revealed that narrower metallic patches exhibit lower phase agility; as a consequence, varactor diodes with wider capacitance variation ranges need to be used. The issue is that such varactor diodes have larger series resistance that might completely outweigh the benefit of a smaller phase discretization step, such as a lower side lobe radiation level.

By virtue of (4), a discretized RRA phase profile for an RRA composed of periodically arranged subwavelength elements of the width W_{ph} , can be calculated as

$$\varphi_n = \varphi_0 + \frac{2\pi}{D}x_{0,n} = \varphi_0 + n\frac{2\pi}{D}W_{ph} = \varphi_0 + n\Delta\varphi, \quad (5)$$

where $\varphi = 2\pi W_{ph}/D$ denotes the phase increment per RRA element and $D = \lambda_0/(\sin\theta^i - \sin\theta^r)$ represents the spatial period of the phase profile.

The discretized profile obtained according to (5) is not always realizable—the quality of the realization depends on the underlying RRA design. The structure's phase agility (the range of possible phase values that can be achieved with a given design) and non-uniformity of the reflection coefficient magnitude may severely degrade the RRA performance.

The reactance finding procedure adopted in the present study comprises the following steps:

1. Calculate the phase profile period for the desired power reflection angle and incidence angle $D = \lambda_0/(\sin\theta^i - \sin\theta^r)$;
2. Find the required phase increment (difference in phase between any two adjacent phase shifters along the beam scanning direction) $\Delta\varphi = 2\pi W_{ph}/D$;
3. Using $\Delta\varphi$ from the previous step, find a reflection phase value, φ_n , for each phase shifter;
4. Obtain the phase response curve via the full-wave analysis using Ansys HFFS 2023 R1 for a finite RRA model. Namely, the reflected phase of a uniformly configured RRA model with finite dimensions (all elements have the same reactances) is retrieved for different values of the diode reactance in the range from 10 Ω to 100 Ω ;
5. Construct a least-squares-based polynomial approximation of the phase curve using the MATLAB built-in function *polyfit()*. The phase is expressed as a function of the varactor diode reactance;
6. Generate a set of reactance values with a step size of 0.1 Ω and calculate the reflection phase value for each of them using the polynomial approximation;
7. Find the diode reactance values, which ensure the required set of discrete reflection phase values, φ_n , using the following MATLAB R2019b built-in function: *Reactances = inper1(ReflectionPhase, Reactance, RequiredPhaseValues)*.

It is noteworthy that in the ideal case of an infinite periodic surface, only the reflection phase curve slope affects the value of the desired reflection angle. Thus, an arbitrary constant phase term can be added to the reflection phase profile without affecting the results. However, this may be different for finite RRAs. For this reason, simulations were

performed for different values of the constant phase term to find the one giving the best radiation pattern.

2.4. Proposed RRA Design

The proposed RRA design employs electronically tunable subwavelength resonators as phase shifters. Each phase shifter is formed by a pair of long and narrow (extended in the azimuthal plane) 8-shaped metal patches printed on an FR-4 PCB. The phase shifters are identical in shape and size. The PCB is backed by a thin copper sheet serving as the ground plane. The purpose of the metallic sheet located behind the phase shifter layer (PCB) is twofold. First, it acts as a screen that substantially suppresses backscattered fields. Additionally, it increases the phase shifter's total inductance, resulting in a lower resonant frequency for the same patch dimensions. Also, each phase shifter has a pair of narrow metallic strips needed to ensure electrical contact between SMD varactor diodes and the 8-shaped metallic patches.

The choice of the RRA design is dictated by practical considerations and substantiated by findings of an extensive numerical study of various RRA phase shifter (metal patch) configurations carried out for an infinite RRA model described in what follows. The study aimed at minimizing the reflection magnitude variation (closer to the uniform one) while maintaining a sufficiently wide reflection phase range. Additionally, the phase shifter dimension (width) along the beam scanning direction was constrained during the study to minimize the phase profile discretization error, leading to increased side lobes.

The following phase shifter configurations were examined: two solid patches (capacitive patches), O(D)-shaped patches, and C-shaped patches. It was found that the solid patches exhibited the worst behavior, as the magnitude exhibited a large dip in the vicinity of the resonance. The O-shaped patches gave better results, owing to additional inductances due to the narrow strips obtained by introducing a rectangular window to each metal patch. Regarding the C-shaped patches, they showed slightly larger phase variation than their O-shaped counterparts.

Finally, based on the observation that the gap between the adjacent phase shifter patches in the same column has little effect on the RRA behavior, a decision was made to combine two adjacent pairs of O-shaped patches, which resulted in the 8-shaped configuration. To be more specific, combining the O-shaped patches only slightly affects the magnitude and phase responses. At the same time, 8-shaped (combined) patches require fewer biasing wire pairs (half the number of wires in the O-shaped patch-based design), which further reduces the adverse effect of the biasing lines on the RRA efficiency. In this configuration, the same voltage is applied to the pair of diodes mounted on a phase shifter via two wires, each connected to a respective 8-shaped patch of the phase shifter.

A similar two-layered RRA unit cell design was recently proposed and numerically analyzed in [64], where the reflection phase adjustability was also achieved using varactor diodes. However, the RRA presented [64] was designed to operate at a much higher frequency than that of the RRA presented herein, namely in the C-band (5.1 GHz). While conceptually similar, the physical and technological constraints imposed on the RRA operating at 865.5 MHz and 5.1 GHz differ significantly; therefore, the challenges also differ. Specifically, the main bottleneck of an RRA operating is a narrow varactor diode capacitance range. Furthermore, the RRA described in [64] is intended for a different application—pencil beam forming, not WPT.

The operating principle of the phase shifters adopted in this study is as follows. The electric field component of an incident electromagnetic wave induces a current on the surface of the metal patches. The fact that the shape of the total scattered wave depends on the amplitudes and phases of the patch currents enables one to locally adjust the phase and amplitude of the scattered wave as well as change its shape, e.g., one can achieve a plane wave propagating in a desired direction. The tunability is achieved by applying different voltage levels to different diodes, which enables one to reconfigure each phase shifter independently.

First, a single-unit cell model is constructed to determine the reflection coefficient's phase and amplitude at different varactor reactance values. The unit cell model containing only one 8-shaped phase shifter is built and analyzed using full-wave solver Ansys HFSS 2023 R1. Applying Floquet boundary conditions to two pairs of opposite unit cell faces results in a 2D periodic reflecting surface model. More specifically, the scattered fields calculated within the unit cell with the periodic boundary conditions correspond to those produced by an infinite array composed of identical unit cells arranged in a contiguous manner periodically along the x - and y -axis. Figure 2 depicts an Ansys HFSS model of a single-phase shifter.

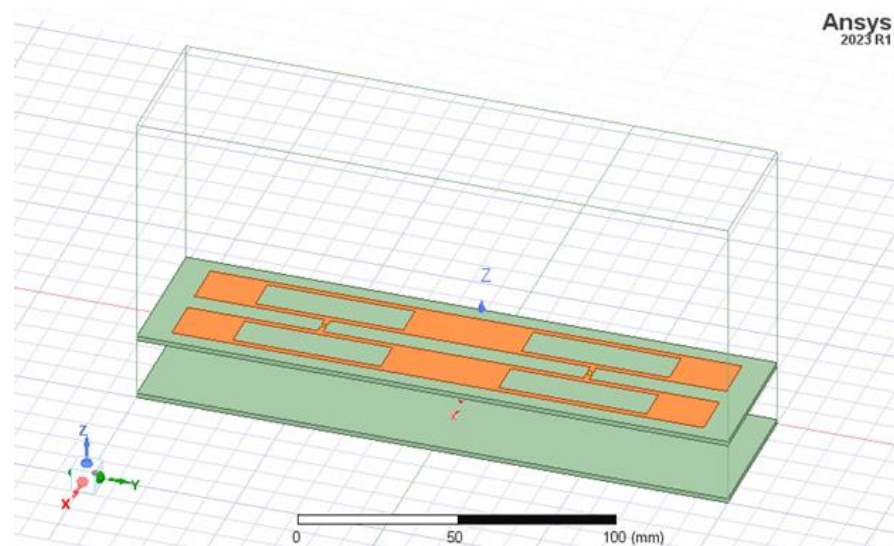


Figure 2. Ansys model of the RA unit cell.

The dimensions of the unit cell, as well as other unit cell parameters, are presented in Table 1. This approach imitates an infinite RA analysis method relying on the Floquet–Bloch theory, as described in [65]. A Floquet port was added to excite an incident TM plane wave and retrieve both the amplitude and phase response curve.

Table 1. RRA phase shifter (unit cell) parameters.

Parameter	Symbol	Value
Unit cell width	W_{ph}	90 mm
Unit cell length	L_{ph}	50 mm
8-shaped patch width	W_{out}	16 mm
8-shaped patch length	L_{out}	90 mm
Separation between the patches	g	7 mm
Patch slot width	W_{in}	12 mm
Patch slot length	L_{in}	50 mm
Transverse strip width	W_s	2 mm
Diode gap	l_p	1.5 mm
Longitudinal strip width	w	2 mm

The diodes are modeled as linear lumped elements. The EM simulation software (Ansys HFSS 2023 R1) used in this study offers two ways of approximating linear lumped elements. One can either substitute a Lumped Port object (or Circuit Port object) for each varactor diode or use an RLC Lumped object. The difference between these two approaches is in the way the fields are approximated on the object faces. The use of port objects requires less finite elements to discretize the fields on their faces as they are uniformly distributed. The RLC Lumped elements, by contrast, exploit impedance boundary conditions; as such, the fields on their surfaces may, in general, be arbitrary [66].

The results presented in this paper were obtained using Lumped Ports only to model varactor diodes. However, numerical tests performed by the authors show that the choice of the diode approximating model slightly affects the results. A more in-depth analysis of this issue will be conducted in our future research. The RRA unit cell model parameters are shown in Figure 3.

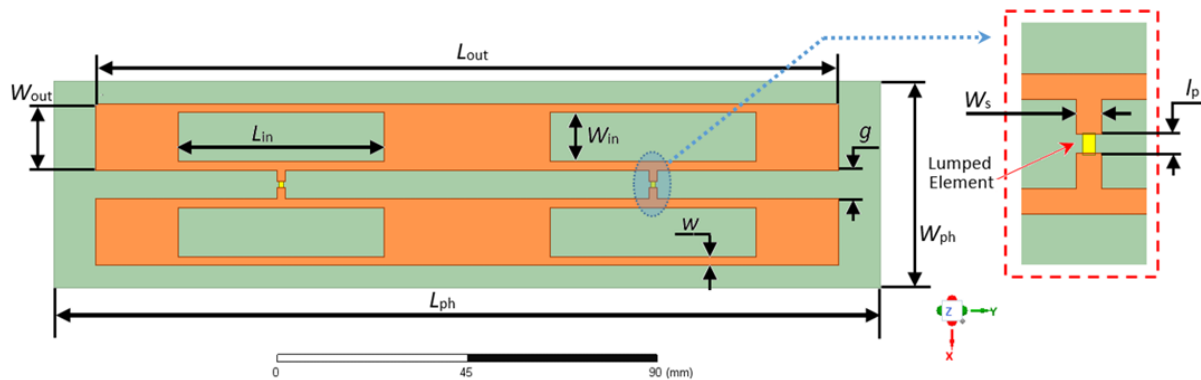


Figure 3. Ansys model of the RA unit cell (top view).

3. Numerical Results

Figure 4 shows the reflection coefficient phase as a function of the varactor diode reactance calculated for an infinite RRA (using the Periodic Floquet boundary conditions—Primary/Secondary pair in Ansys HFSS). Each curve from the curve family presented in the figure corresponds to a distinct value of the separation distance between the upper substrate containing the phase shifters and the ground plane (inter-layer separation). In this case, the ground plane is formed by several FR-4 PCBs whose front faces are fully covered by a thin metal layer. Figure 5 plots a family of the reflection coefficient magnitude versus the reactance curves found for the same inert-layer separations. This allows one to assess the relation between the behavior of the phase response and the amplitude response.

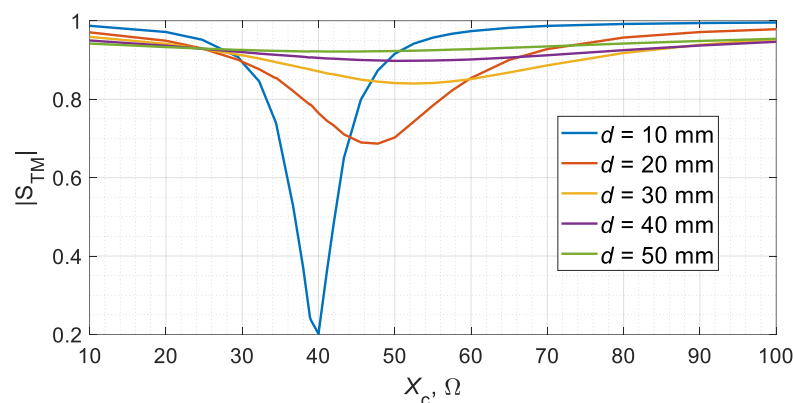


Figure 4. The reflection coefficient phase as a function of varactor reactance calculated at different separations between the upper and the lower layers of infinity periodic RRA model.

It is observed that all the phase curves are similar in shape but differ in the rate at which the phase varies with the varactor diode reactance. Also, the variation rate decreases as the inter-layer separation increases. In addition, the curves exhibit the highest slope in the vicinity of the resonance. On the one hand, the curves with higher slopes demonstrate larger differences between the minimum and maximum phase values (better phase agility) achievable for the same range of varactor capacitance and, therefore, are more advantageous from the RRA realizability standpoint. However, a higher phase curve slope comes at the cost of an increased variation in the reflection coefficient magnitude value. This variation should be as small as possible since, according to the GGO theory used as the primary

method in the present study, the magnitude must be as uniform as possible to ensure adequate phase profile approximation. Otherwise, the radiation pattern of the RA will have large side lobes.

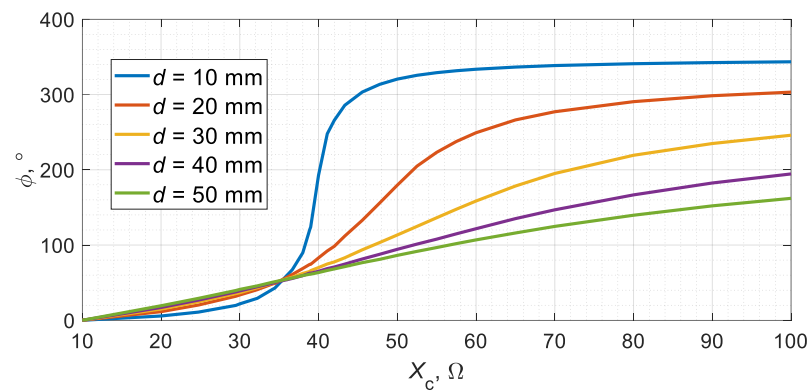


Figure 5. The reflection coefficient magnitude as a function of varactor reactance calculated at different separations between the upper and the lower layers of infinity periodic RRA model.

Using thicker substrates reduces the magnitude variation but requires more dielectric material. This issue can be mitigated by using a two-layer configuration in which one of the layers (phase shifting layer) is a dielectric substrate (PCB) with a number of planar metallic phase shifters printed on its top face, while the other one is just a flat copper sheet. This aspect motivated the authors to select a two-layer RRA configuration for the present study. Such a structure can also be regarded as a three-layer one, where the intermediate layer is an air layer. The presence of the air layer adds a degree of freedom and, as can be seen, allows the reduction of the overall losses and the magnitude variation. The magnitude variation results from the losses of the PCB dielectric material, metal patches, ground plane, and varactor diode. Also, the magnitude is affected by the finite dimensions of the RA.

Hence, the two main limiting factors to be considered are phase agility and non-uniformity of the amplitude response. As evidenced by Figures 4 and 5, the uniformity of the amplitude response can be improved by increasing the inter-layer separation. It is clearly seen that the reflection coefficient amplitude obtained for the infinite model with $d = 4$ cm does not exhibit such large variation as that of the RRA with identical unit cell parameters, except d , which in this case is 2 cm. The amplitude response in the case of $d = 2$ cm exhibits a sharp dip at the value of X_c at which the resonant frequency of the RRA phase shifters becomes equal to the operating frequency (865.5 MHz). However, improving the amplitude response in this way comes at the expense of reduced phase agility of the RRA, as follows from the phase curves shown in Figure 5. Indeed, the difference between the minimum and the maximum reflection coefficient phase values achievable by varying X_c from 10 to 100 Ω decreases appreciably with increasing d .

The model of the uniformly configured RRA is constructed and simulated at different Lumped port impedance values. The real part of the element impedance is set to 1 Ω , though the value given in the diode's datasheet is just 0.5–0.7 Ω [67]. For convenience, the varactor diode parameters are given in Table 2.

Table 2. Varactor diode SMV1763 parameters.

Parameter	Symbol	Value
Series resistance	R_d	0.7 Ω
Junction capacitance	C_j	1.8 pF (at 0 V)—9 pF (at 5 V)
Parasitic capacitance	C_p	1.42 pF
Lead inductance	L_d	0.45 nH

The reason behind overestimating the diode series resistance is that the resistance value provided by the manufacturer is an equivalent resistance introduced to account for bondwire and lead ohmic losses, as well as losses due to the skin effect that cannot be neglected at sub-GHz frequencies. However, there are also parasitic effects associated with the soldering quality, which also contribute to the overall losses. Furthermore, due to manufacturing tolerance, the diode parameters vary from one device to another. This variability in the parameter values also contributes to the degradation of RRA performance. Regarding the diode model, to realize the proper tunability of the RRA under study, SMV1763 (Skyworks Solutions Inc., Irvine, CA, USA) varactor diodes were selected, as they provide an acceptably wide capacitance tuning range while having sufficiently low equivalent series resistance. Based on the equivalent circuit presented in [67], the equivalent impedance of the diode at frequency f can be calculated as

$$Z_c = R_c + jX_c = \frac{1}{1/(j\omega C_j) + R_d} + j\omega L_d \quad (6)$$

where R_d is the diode equivalent series resistance, L_d is the diode lead and bondwire inductance, C_j is the voltage-dependent diode junction capacitance, and C_p is the diode's linear parasitic capacitance.

Substituting the C_j values corresponding to the minimum and maximum voltages given in Table 2, one finds that by varying the voltage across the diode, one can vary its reactance in the range from about 16.5 to 97 Ω .

3.1. Finite RRA Model

The infinite periodic model is very convenient to handle, as one just needs to calculate the fields within a single unit cell owing to the Floquet theory. On the other hand, one should not expect that the results obtained in this manner will agree well with those obtained for an RRA containing a finite number of cells unless a very large RRA involving hundreds of phase shifters is used. Therefore, it is essential to ascertain the difference in the performance between the ideal RRA and its finite counterpart, as this allows one to adjust the parameters of a finite RRA before fabricating prototypes.

To determine whether the chosen number of elements (RRA size) is sufficient to ensure proper RRA performance, an RRA model comprising a finite number of elements is created and analyzed using explicit full-wave simulations (no approximations are used). The constructed finite array model comprises 36 cells arranged in 2 rows, each containing 18 elements. The Ansys HFSS model of the finite RRA under study is illustrated in Figure 6.

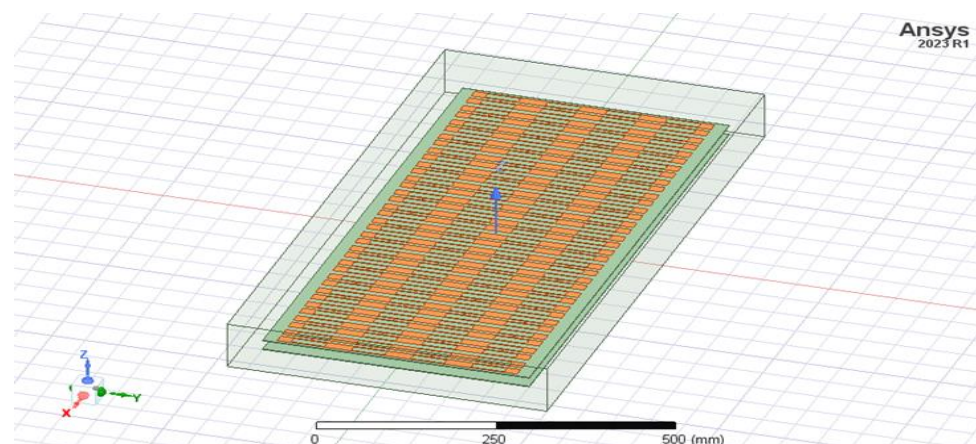


Figure 6. The Ansys HFSS model of RA composed of 36 (18×2) FR-4 phase shifters, each consisting of two diode-loaded metallic 8-shaped patches (tunable surface resonators).

Again, to simulate the unbounded space, absorbing boundary conditions (radiation boundary conditions) are assigned to the surface of the bounding box. The metal patches and the ground plane are modeled as 2D objects with the impedance boundary conditions applied to account for the conduction losses. The dielectric losses are also taken into account. The parameters of the RRA under study are presented in Table 3.

Table 3. Parameters of a single RRA panel.

Parameter	Value
Panel width	200 mm
Panel length	300 mm
Upper substrate thickness	1.55 mm
Lower substrate thickness	1.55 mm
Inter-layer separation	20–40 mm
Substrate material	FR-4 ($\epsilon_r = 4.4$, $\tan\delta = 0.02$)

Figure 7 compares the phase curves of infinite and finite RRAs calculated at different inter-layer separation values, from 2 cm to 4 cm at an increment of 1 cm. In all cases, the finite RRA phase curves have slightly lower slopes in the vicinity of the resonance. Nonetheless, the curves are very close. The difference occurs due to the edge effect present in finite arrays only.

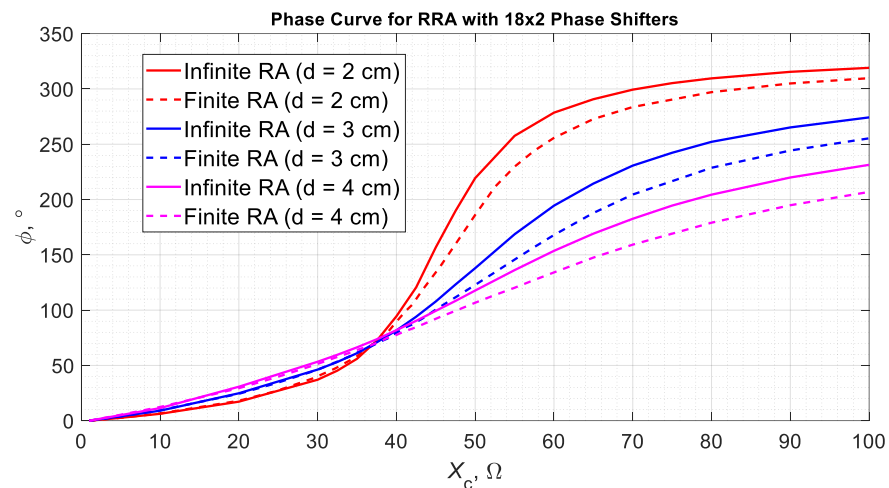


Figure 7. The phase curves calculated at different diode reactance and inter-layer layer separation distances for an infinite RRA model and a finite model consisting of 36 (18×2) phase shifters.

Additionally, two farfield patterns showing the behavior of normalized electric field intensity of the scattered wave at a distance much larger than a wavelength are calculated. To obtain the farfield pattern, the RRA is illuminated by an incident plane wave impinging normally on the structure's surface. Again, the RRA is configured to have uniform phase profiles with different values of the reflection phase, which is controlled by varying the element reactances. The RA is composed of 6 (3×2) identical panels constructed from FR-4 PCBs. Figure 8 shows the computed farfield patterns for the finite RRA model calculated at $d = 2$ cm and $d = 4$ cm. The figure reveals that for the surfaces containing 18×2 phase shifters, the radiation pattern shape does not vary markedly with the diode reactance value, corroborating a common assumption made in the channel performance prediction of IRS [68]. Namely, the radiation pattern of small unit cells may be regarded as being close to that of a finite metallic patch when calculated by means of the Physical Optics Approximation [69].

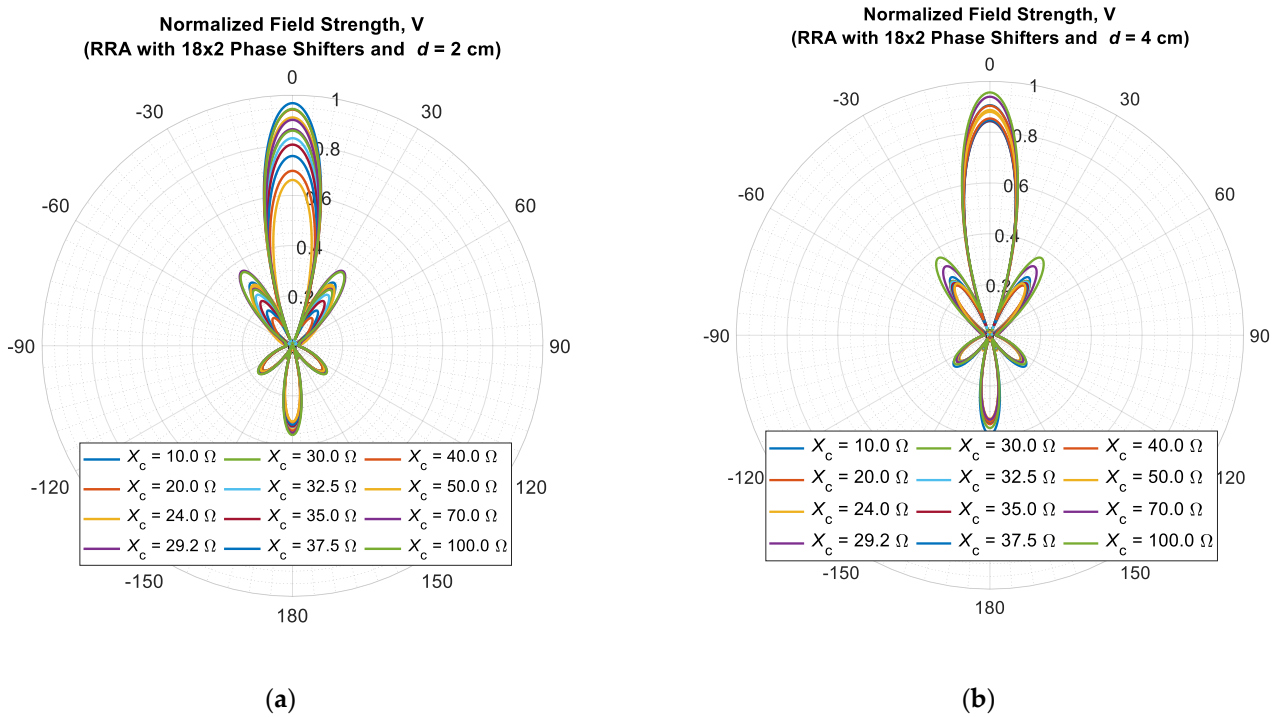


Figure 8. The farfield pattern in the azimuthal plane of the RA model with 18×2 varactor diode-loaded 8-shaped phase shifters computed at different diode reactance values in the range from 10 to 100Ω when the inter-layer separation is 2 cm (a) and 4 cm (b).

3.2. The Indoor Environment under Study

Now, let us examine the performance of the RRA with phase profiles designed to steer the reflected power beam toward directions other than the specular one. For this purpose, a phase profile ensuring the required reflection angle is derived using the GO-based approximation. Then, the values of the reflection coefficient phase are calculated using (5). Finally, the phase shifter reactances that ensure the required local phase shifts are retrieved from the phase curve data obtained for the uniformly configured RRAs with finite dimensions (see Figure 8).

The RRA to be examined is geometrically identical to that analyzed in the previous subsection; namely, it consists of 3×2 identical panels, each containing a single phase-shifter row with six elements. However, in contrast to the study of the uniformly configured RRA, a model closer to the real-life WPT scenario is considered in this case.

The model involves two Yagi antenna models alongside the RRA model itself. The transmitting and receiving antennas are assumed to be identical printed 4-element Yagi antennas with a maximum gain of 9.17 dBi. The antennas are located at the same height of 1 m. The distance between the IRS panel and the transmitting antenna is fixed and assumed to equal 1.5 m.

Here, only the RRA model is analyzed explicitly using Ansys HFSS to reduce the CPU time. The contribution of the Yagi antennas is calculated using the experimentally measured antenna gain. The incident wave is assumed to be a plane wave since the distance between the transmitting antenna and the RRA front face is about 4.4 wavelength.

The electric field on the RRA surface produced by the transmitting Yagi antenna can be expressed as [70]

$$|\Pi_{\theta}^i| = \frac{P_{tx}}{4\pi d_{tx-RRA}^2} = \frac{|E_{\theta}^i|^2}{2Z_0} \Rightarrow |E_{\theta}^i| = \sqrt{\frac{Z_0 P_{tx}}{2\pi d_{tx-RRA}^2}} \approx \frac{\sqrt{60 P_{tx}}}{d_{tx-RRA}}, \quad (7)$$

where E_{θ}^i is the electric field intensity on the RRA surface produced by the transmitting antenna, Π_{θ}^i is the Poynting vector's θ -th component of the wave impinging on the RRA, P_{tx} is the amount of power transmitted by the TX antenna, d_{TX-RRA} is the distance from the phase center of the transmitting Yagi antenna and the central point of RRA, λ_0 is the free space wavelength at the operating frequency, $G_{rx,max}$ is the maximum gain of the receiving antenna, and Z_0 is the free space impedance.

Knowing the electric field intensity on the RRA radiated by the transmitting antenna and the reflectance of the RRA, the received power can be calculated as

$$P_{rx} = \Pi_{\theta}^r A_{eff} = \frac{|E_{\theta}^r|^2}{2Z_0 d_{RRA-RX}^2} A_{eff} = \frac{|E_{\theta}^r|^2}{2Z_0 d_{RRA-RX}^2} \frac{G_{rx,max} \lambda_0^2}{4\pi} = \frac{G_{rx,max} R_{RRA}^2(\theta_{ref}) |E_{\theta}^i|^2 \lambda_0^2}{8\pi Z_0 d_{RRA-RX}^2}, \tag{8}$$

where E_{θ}^r is the electric field intensity on the RRA surface produced the transmitting antenna, Π_{θ}^r is the θ -th components of the reflected wave Poynting vector, P_{rx} is the received power, d_{RRA-RX} is the distance between the central point of RRA and the receiving Yagi antenna phase center, $G_{rx,max}$ is the maximum gain of the receiving antenna, $R_{RRA}(\theta_{ref}) = |E_{\theta}^r / E_{\theta}^i|$ is the reflectance of the RRA at θ_{ref} , and A_{eff} is the effective aperture of the receiving antenna.

The calculated radiation patterns for different uniform RRA configurations are shown in Figures 9 and 10. The radiation patterns were obtained for an RRA model with finite dimensions configured to achieve the radiation pattern peak (received power maximum) at different angles.

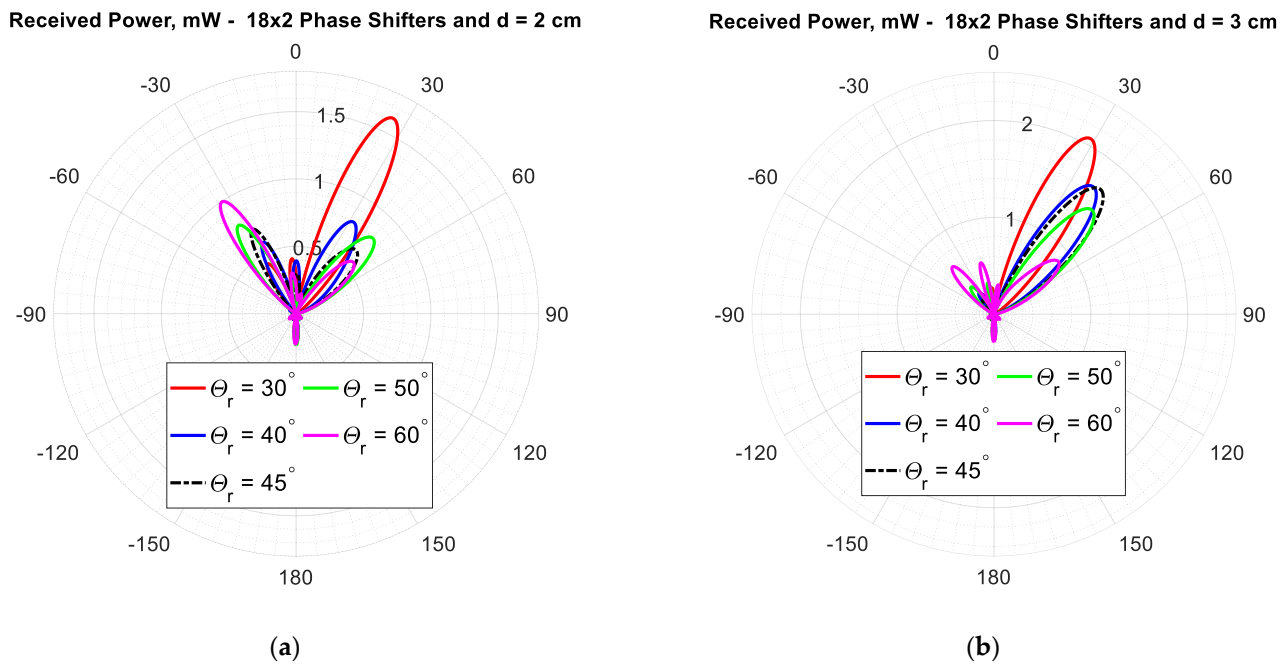


Figure 9. The calculated radiation pattern (Rx power in mW) in the azimuthal plane of the RRA consisting of 36 (18 × 2) phase shifters optimized for different reflection angles with $d = 2$ cm (a) and $d = 3$ cm (b).

First, the RRA's phase profile was synthesized to obtain the peak reflection toward the observer located at an angle of 30° with respect to the RRA surface normal line. Then, the same procedure is applied to steer the beam at 40° , 45° , 50° , and 60° . The radiation patterns obtained for an RRA model containing 36 elements arranged in two rows with 18 elements in each are shown in Figure 9a. As can be seen, only for the RRA configured to steer the beam by 30° , the simulated peak reflected power direction is close to the desired one being equal to 27° . In this case, the amount of reflected power is also relatively high—about 1.615 mW. Meanwhile, the efficiency is substantially lower for the other angles, declining

rapidly as the reflection angle increases. The only exception is the configuration for 50° —in this case, the received power is close to that of 40° RRA. Additionally, even for the 40° RRA configuration, the difference between the actual and desired angles is around 8° . The result clearly shows that the RRA with $d = 2$ cm fails to ensure high wireless powering efficiency in real-life applications.

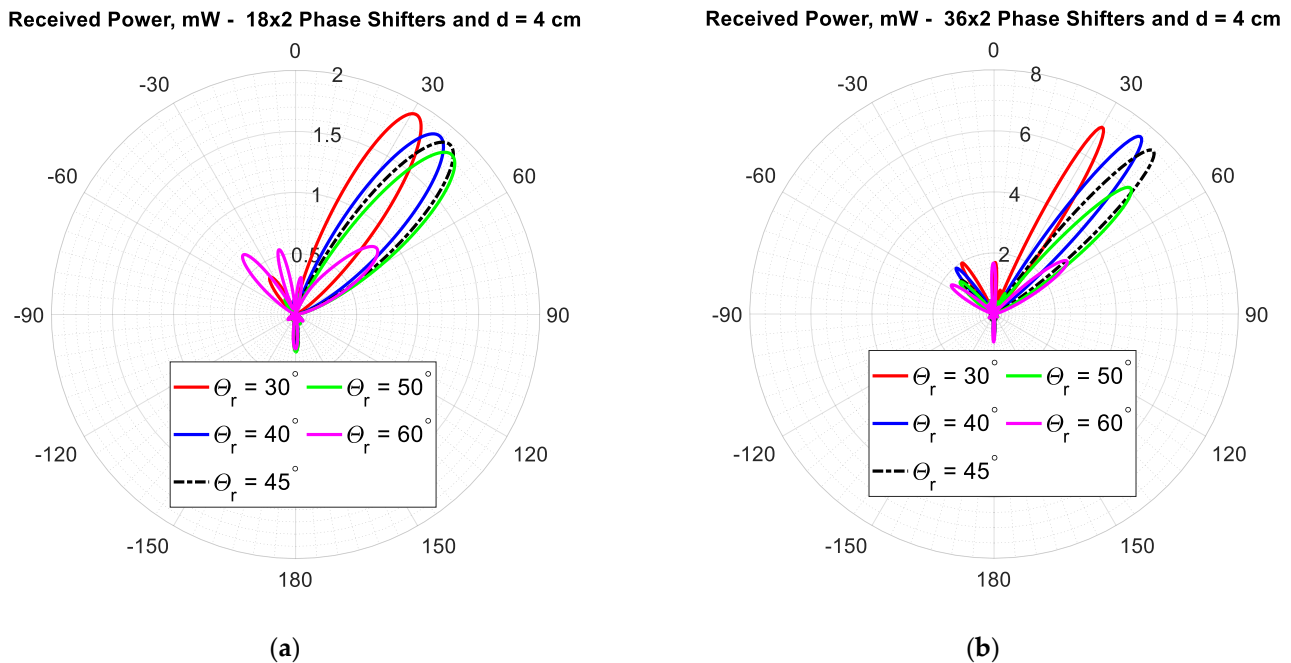


Figure 10. The calculated radiation pattern (Rx power in mW) in the azimuthal plane of the RRA consisting of 18×2 (a) and 36×2 (b) phase shifters with $d = 4$ cm configured for different reflection angles.

Figure 9b presents the radiation patterns calculated for the same RRA but with a larger inter-layer separation ($d = 3$ cm). It is observed that the side lobe level for this RRA is appreciably lower than that of the RRA with $d = 2$ cm. Furthermore, for the first two configurations ($\theta_r = 30^\circ$ and $\theta_r = 40^\circ$), the deviation of the obtained reflection angle from the desired is within 1.5° . For larger angles, this deviation increases with the reflection angle, reaching 10° for the RRA designed to rotate the beam by 60° (the simulated value is 50.5°). For this extreme reflection angle, the amount of received power is much lower than that of the others. Also, the figure reveals that the received power differs only slightly for the reflection angles within the range from 40° to 50° .

The RRA design with $d = 3$ cm demonstrates higher reflection efficiency for angles between 40° and 50° . The angle deviations in this case are comparable to those of the RRA with $d = 3$ cm. However, the pattern presented in Figure 10a exhibits a pronounced side lobe in the mirror direction (at -30°). This sidelobe results from the phase agility not being 360° . The numerical results show that reducing the phase profile period along the reflectarray surface results in larger side lobes, thereby increasing the amount of wasted power. The undesirable side lobes can be reduced by increasing the separation between the RRA layers. Like in the two previous cases, the efficiency of the RRA configured to have an angle of reflection of 60° is very low.

The last set of RRA radiation data obtained by means of the GO-based approximation is presented in Figure 10b.

In contrast to the previous cases, the size of the RRA is twice as large in the azimuthal plane, which should result in an increased amount of the reflected power toward an intended receiver. The main lobes for the RRA composed of 36×2 phase shifters are approximately two times narrower, which agrees well with the antenna theory. The

received power level is by a factor of 3 greater than for the 18×2 configuration with $d = 3$ cm. This can be explained by a larger reflecting antenna aperture area, which results in a larger amount of incident wave power intercepted by the RRA surface. It should be noted, however, that these results have been obtained under plane wave approximation, while in real-life scenarios, narrow beam antennas are used, resulting in a high field intensity spot in the central part of the RRA and lower intensity close to its edges. Additionally, the wavefront of narrow beam antennas, such as the ones utilized in the experimental part of this study, is close to that of the plane wave only at relatively large distances between the antenna and the RRA.

3.3. Floquet Mode-Based RRA Synthesis Approach

As has been seen before, for large reflection angles ($>45^\circ$), the classical approach employing the generalized GO approximation fails to ensure high power reflection efficiency. The reason is that RRA configurations synthesized using the above method exploiting GO approximation at large reflection angles exhibit high side-lobe levels. Some authors point out that for specific RA designs, the conventional method can only guarantee sufficiently high efficiency for deflection angles smaller than 30° . This issue arises due to the natural limitation of the GO-based theory. Namely, within the GO framework, the contribution of surface waves on any periodic surface to the power balance and, therefore, the power profile across the surface is completely ignored. For small angles, the method still provides sufficiently accurate results due to the fact that the effect of the surface waves is negligible for a large phase profile period to the phase discretization step (phase shifter size) ratio [71].

Nevertheless, in some cases, it is still possible to achieve large beam scan angles without sacrificing power conversion efficiency [72]. In order to accomplish this, one must ensure a periodic power flow into the RRA structure and back into space. For instance, in the case when both the incident and reflected waves have equal amplitudes, an RA performs the desired function perfectly; however, the power profile along the surface of the reflector is strongly nonlocal. To be more specific, some parts of the RA absorb the power of the incident wave ($P_{\text{RRA}} < 0$), whereas the other parts radiate the power needed to form a plane wave traveling in the desired direction ($P_{\text{RRA}} > 0$). The average power over the surface must be equal to zero. Alternatively, the perfect reflection can be achieved if the metasurface comprises both absorbing and radiating elements while being overall lossless.

The most straightforward way to overcome this limitation of the GO-based method is to directly apply the Floquet mode theory to the phase profile synthesis by finding an appropriate surface impedance profile. Again, due to the finite dimensions of the phase shifters, it is possible to obtain only a discretized surface impedance. Despite its great flexibility, this method is highly computationally intensive, which substantially limits its use. The reason is that it cannot find the required phase shifter impedance values using closed-form expressions. Although this can be accomplished by means of various optimization techniques, in many cases, the optimization process requires significant computational resources.

In the case of low-loss RAs, the surface impedance profile can be obtained by applying an optimization procedure to its idealized counterpart (loss-less model) [60]. The optimization objective is to maximize the amplitude of the surface Floquet mode corresponding to the plane wave reflected in the desired direction. Proceeding in this way will automatically reduce the amplitudes of the unwanted Floquet modes, leading to reduced side lobe levels. At the same time, the impedance profile maximizing the power reflected in the desired direction will ensure the lowest possible losses in the RA.

Notably, ref. [73] describes a more time-efficient alternative to the explicit Floquet mode analysis. The method extends the GO-based method by introducing fictitious auxiliary surface waves. The auxiliary waves satisfy Maxwell's equations and Generalized Sheet Transition Conditions (GSTC) [74], which implies that such a structure is physically realizable. It has been shown that the use of these waves can, to a certain degree, mitigate the large deflection angle limitation of RAs.

In this study, to ascertain whether it is possible or not to achieve extreme reflection angles ($>60^\circ$) using the developed RRA design, the Floquet theory-based optimization is employed. An auxiliary wave-based approach will be attested in our future studies. This approach exploits some properties of Floquet modes that are excited in any periodic structure. The number of propagating Floquet modes depends on the wavelength and the spatial structure period—the length of the supercell (a set of unit cells with different reactances that are periodically repeated along the beam scanning direction).

Under normally incident plane wave excitation, there may exist more than one reflected plane wave (propagating Floquet mode)—the number of these waves and propagation directions depends on the ratio D/λ_0 . The other Floquet modes are surface modes that cannot carry power away from the RRA surface.

Since the dimension of the supercell in the elevation plane is smaller than the wavelength at 865.5 MHz, only modes with $n = 0$ can propagate. The angle at which the (m -th, 0 -th) mode, regardless of the polarization (TE or TM), travels away from the RRA is given by

$$\theta_{m,0} = \tan^{-1} \left(k_x / \sqrt{k_0^2 - k_x^2} \right) = \tan^{-1} \left(m / \sqrt{(D/\lambda_0)^2 - m^2} \right). \quad (9)$$

To facilitate the optimization process, the chosen optimization algorithm is applied to a lossless RRA model that is otherwise identical to the original supercell model. This assumption may accelerate the algorithm convergence and establish theoretical limits on the RRA efficiency at reflection angles larger than those governed by the GGO. The optimization is applied to a model containing an integer number of cells whose length is an integer multiple of a phase profile period. An idealized lossless model was optimized before optimizing a more realistic model that accounts for both conductor and dielectric losses to reduce the computational burden.

Two cases were examined, showing that large beam-scan angles can be achieved by the Floquet theory-based analysis. The proposed RA is a two-layered structure. One layer contains electronically tunable resonators, whereas the other is fully covered by metal to increase the inductance of the resonators and reduce power radiation in the backscattering direction. To that end, the virtual infinite array of supercells was optimized using one of the Ansys HFSS 2023 R1 built-in optimization algorithms (Adaptive Multi-Objective (Random Search)). Each cell of the infinite array contained an integer number of phase shifters (supercell) chosen according to the Floquet theory. The radiation patterns showing the amount of received power per supercell (total power/number of supercells) are depicted in Figure 11.

The patterns of RRA consisting of 8 phase-shifters and optimized to have the maximum magnitude of the TM_{10} Floquet mode propagating at about 60° obtained for different numbers of supercells are plotted in Figure 11a. The patterns shown in Figure 11b were computed for the RRA with 7 elements per supercell, resulting in the desired reflection angle of 80° . In both cases, the losses were taken into account.

The results obtained by means of the Floquet-based RRA synthesis approach allow one to find such RRA diode reactances that can deflect the beam by up to 80° . By contrast, the generalized reflection law (Generalized Geometrical Optics Approximation) based approach can ensure adequate RRA performance only for relatively small angles (up to about 40 – 50°). Unfortunately, the theoretical analysis based on the Floquet theory is substantially more computationally intensive—the reactance value optimization was performed on a machine with 256 GB RAM and several Intel family processors with a total of 64 cores. Performing a similar RRA design would be prohibitively long due to the need for real-life measurements instead of calculations. For this reason, the authors abandoned the idea of performing Floquet Theory-based RRA configuration in the experimental part of the present study.

Moreover, the normalized radiation pattern shown in Figure 11 reveals that even though the proposed design is theoretically capable of forming a narrow beam at such extreme angles as 80° , the power reflected per a single supercell is so small that a more

or less adequate reflection efficiency can be ensured when the dimensions of the RRA are comparable with those of typical indoor environment, e.g., an office room, which would make the use of such large RRAs entirely impractical.

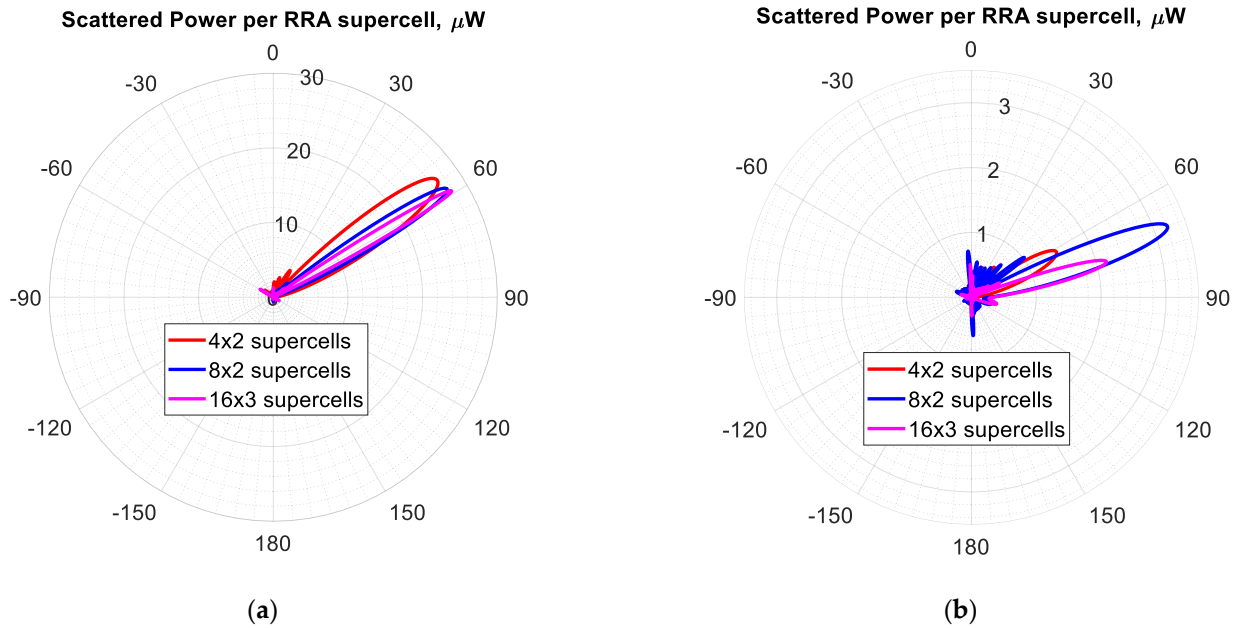


Figure 11. The normalized calculated radiation pattern (received power in mW over the phase shifter number squared in the case of plane wave excitation with the electric field intensity of 1 V/m) in the azimuthal plane of the RRA optimized using the Floquet theory-based synthesis method for a desired reflection angle of 60° (a) and 80° (b).

4. Experimental Verification and Optimization

A prototype consisting of 36 8-shaped varactor diode-loaded metal patches acting as tunable phase shifters was fabricated and measured to experimentally verify the effectiveness of the developed RA unit cell design. Figure 12 presents photos of the prototype. The phase shifters are formed by a milling machine available at the faculty laboratory on a standard FR-4 PCB utilized as the upper layer of the RA. A total of 6 such FR-4 PCB-based panels were created. All panels feature layouts that are identical to within the machining tolerance of the milling machine. The dimensions of the 8-shaped phase shifters are the same as in the case of the 36-element model described above (see Table 1).

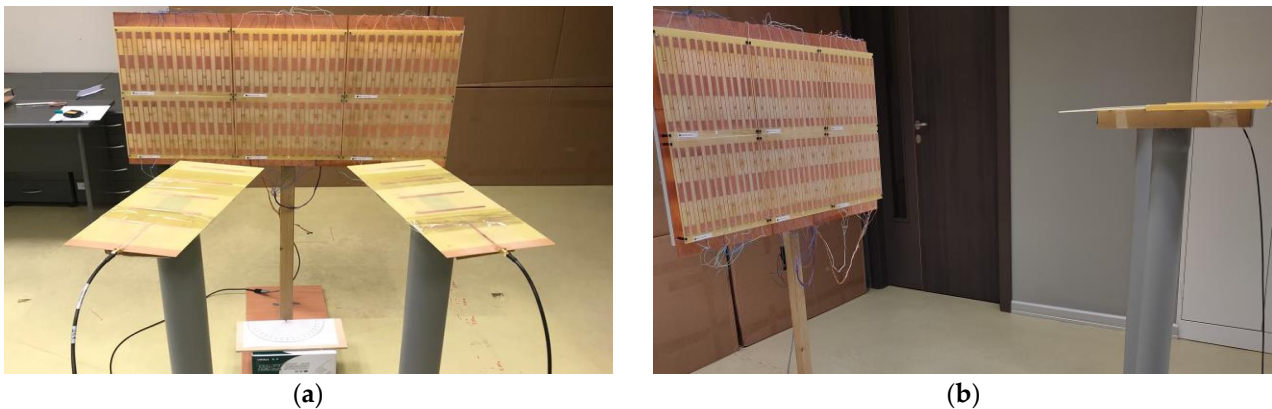


Figure 12. The experimental setup composed of the RRA under study and two Yagi antennas arranged for the measurement of phase curve (a) and for the RRA optimization for the desired reflection angles of 30° (b).

The varactor diodes mounted on the phase shifters of the RRA prototype are the same as those treated in the theoretical analysis, namely, SMV1763. However, in contrast to the numerical analysis, the diodes used in experiments, like the vast majority of other semiconductor components, exhibit quite large parameter deviations from the mean values stated in the relevant documentation. The parameter variation may lead to significant RRA efficiency degradation and, therefore, be taken into account. To compensate for the effect of parameter tolerance on the RRA performance and mitigate the influence of the biasing network, an experimental optimization is performed in real time to find the experimental voltage combination giving the maximum achievable received power.

A signal generator Rohde-& Schwarz SMR30 cascaded by a custom-made two-stage amplifier was used to ensure a power level of 0.3 W at the input of the TX Yagi antenna. A digital oscilloscope Tektronix DPO72004C was employed to measure the power delivered to the TX antenna and the one received by the RX antenna. The power-carrying signal from the output of the second amplifier stage is split into two equal components by means of a standard coaxial splitter. One of the splitter outputs is connected to the TX antenna to deliver 0.3 W power to it, whereas the other portion is fed to the oscilloscope to measure the amplifier output power.

The experimental setup designed for RRA characterization allows one to control the voltage across each varactor diode pair separately, thus providing great configuration flexibility and making the optimization process more efficient. Figure 13a presents a photo of the measurement equipment, which includes the signal generator, the oscilloscope, and the two-stage high-frequency signal amplifier, which is equipped with fans to prevent the amplifier's second stage from overheating. Figure 13b illustrates the Yagi antennas arranged to measure the reflected power pattern resulting from the normal illumination of a medium-sized metallic sheet.

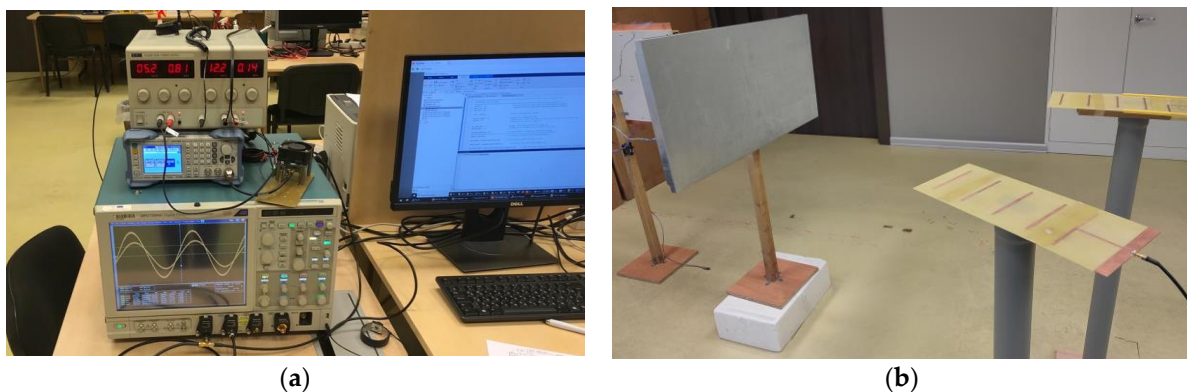


Figure 13. The measurement setup comprising a custom made two stage RF signal power amplifier, digital oscilloscope Tektronix DPO72004C, and Rode-Schwarz SMR30 RF signal generator (a) and the experimental Yagi antenna arrangement intended for the measurement of the reflected power pattern of a metallic sheet (b).

It is noteworthy that, in contrast to the theoretical analysis where the reactances were used to characterize the behavior of each phase shifter, the diode voltages are used instead in the experimental study. The reason is obvious—the RRA controlling board varies diode reactances by applying different reverse voltages to the diodes, which can be measured straightforwardly with a multimeter; as a result, they are more convenient to deal with than the reactances.

For each RRA unit cell (phase shifter), the varactor diode capacitance control is ensured using several 12-bit MCP4728 (Microchip Technology, Chandler, AZ, USA) DACs (Digital-to-Analog Converters). A microcontroller unit (MCU) connected to a PC adjusts the DAC's voltage levels. The MCU outputs are connected to several digital-to-analog converters (DAC) intended to produce and apply required bias voltages to varactor diodes mounted on the metal patches of the RRA. Additionally, a simple lowpass filter is inserted between

the DAC output and the pair of wires to reduce the adverse effect of the parasitic TEM transmission lines formed by the wire pairs connecting the edges of the 8-shaped patches with the DAC outputs.

4.1. Phase Response Measurement

Regarding the RRA configuration, similar to the theoretical analysis conducted above, in the experimental study, the desired discrete phase profile, produced by ensuring certain varactor diode voltage combinations, is also synthesized based on the phase curves. However, for the RRA prototype diode voltage calculation, the experimental curves are used in place of the simulated ones. The reason for this is that various parasitic effects may significantly impact the performance of the RRA. When the element voltages are extracted directly from the measured phase data, the effect of the parasitics is implicitly taken into account.

The RRA's experimental phase response was retrieved using the two-antenna method. During the received power measurement, the RRA was illuminated normally—the TX antenna boresight axis is perpendicular to the RRA plane. The incident wave was produced by a printed Yagi antenna with four directors and a measured gain of approximately 9.17 dBi. The receiving antenna utilized in the measurement was completely identical to the transmitting one. The receiving antenna was positioned so that its boresight would be aimed at the middle point of the RRA, mounted on a fixture (flat wooden board) with wooden support and baseplate. The experimental setup used for the measurement of both the phase curves and the RRA radiation patterns is shown in Figure 12a,b. Both antennas were located 1.5 m away from the front surface of the RRA under study, and the separation between the antennas was about 20–25 cm. In this part of the experimental study, equal voltages were applied across all varactor diodes to establish a uniform phase profile, and the common voltage level was gradually varied from 0 to 5 V, with an increment of 0.2 V. Then, the desired phase was extracted from the measured time delay between the sine wave arriving at the first oscilloscope channel from one of the two splitter outputs and the one coming to the second channel from the receiving antenna.

Following the RRA phase response measurement, small fluctuations and distortions in the obtained phase profile were reduced with the use of a simple Centred Moving Average Filter (CMAF) with a window size of 10 samples. In addition, to further smooth the phase curve, a polynomial interpolation was constructed using a least-squares-based data fitting algorithm (MATLAB R2019b built-in function *polyfit()*). Then, the interpolating polynomial was used to calculate the voltage values, ensuring the desired varactor diode reactances.

It should be noted that the measured phase curves are not quite smooth due to measurement noise and various kinds of interference, even though the oscilloscope itself was configured to measure the mean value of the time delay between the transmitted and received signals. Specifically, the time delay value for each diode voltage level was obtained by measuring the mean value of the time delay several times (5 times) with a certain pause introduced between the successive measurement cycles and taking the average. Furthermore, each measured mean value was automatically calculated by the oscilloscope through averaging over a large sample of measured time delay values.

To summarize, the diode voltage finding procedure is almost identical to that for the calculation of the reactances followed in the theoretical analysis given in Section 2. To find the required diode voltages, the following steps must be taken:

1. Calculate the phase profile period for the desired power reflection angle, assuming the normal incidence $D = \lambda_0 / \sin \theta^r$;
2. Find the required phase increment $\Delta\varphi = 2\pi W_{\text{ph}} / D$, where W_{ph} is the unit cell width;
3. Using $\Delta\varphi$ from the previous step, find the required reflection phase value, φ_n , for each phase shifter;
4. Retrieve the phase response from the values of the time delay between the incident and reflected sine waves measured with the digital oscilloscope for uniformly configured RRA at different voltage levels ranging from 0 V to 5 V;

5. Perform smoothing of the experimental phase curve using a Centred Moving Average Filter (CMAF) with a window size of 10 samples;
6. Construct a least-squares-based polynomial approximation of the phase curve using the MATLAB built-in function *polyfit()*. The phase is expressed as a function of the varactor diode voltage;
7. Generate a set of reactance values with a step size of 0.1 V and calculate the reflection phase value for each of them using the polynomial approximation;
8. Find the diode reactance values, which ensure the required set of discrete reflection phase values, φ_n , using the following MATLAB built-in function: *Voltages = inper1(ReflectionPhase, DiodeVoltage, RequiredPhaseValues)*.

For comparison, both the calculated and the measured phase curves obtained for different inter-layer separations are plotted in Figure 14. As can be seen, the measured and calculated curves obtained at different values of d have similar shapes. Nevertheless, in all three cases examined, the measured curves exhibit higher slopes than the ones obtained by means of Ansys HFSS. The measured reflection magnitude data (not presented herein) shows similar behavior. Namely, the reflection minima observed in the vicinity of the resonant frequency are deeper than in the case of calculated responses. Since the higher diode losses increase the slope of the phase curve and make the magnitude minima deeper and sharper, the observed discrepancy is likely due to underestimated phase shifter losses. Additionally, to improve the fidelity of the RRA model, an equivalent diode resistance can be calculated based on the measured phase curves. The fact that the measured curve for $d = 4$ cm is closer to the calculated curve for $d = 3$ cm suggests that the measured radiation pattern for $d = 4$ cm should be close to the computed one for the RRA with 3 cm.

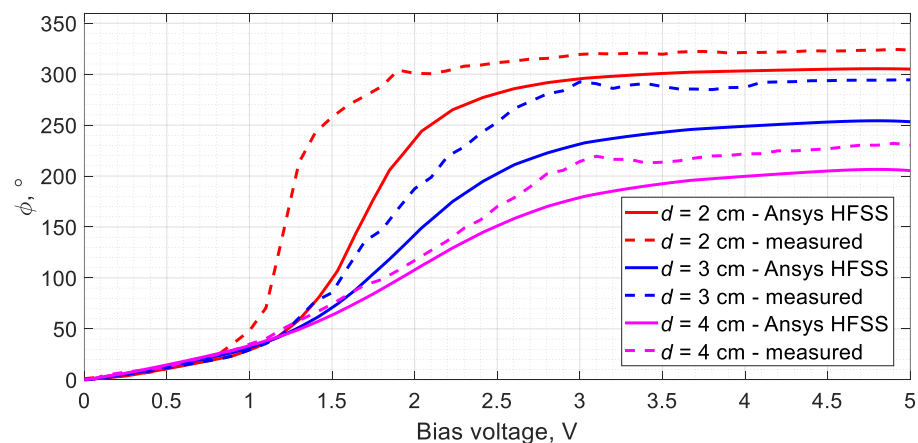


Figure 14. The calculated (solid line) and measured (dashed line) reflection coefficient phase against the diode bias voltage of a uniformly configured RRA consisting of 36 (18×2) phase shifters at different distances between the substrates.

4.2. RRA Optimization and Radiation Pattern Measurement

The next and most crucial step of the measurement process is to obtain the beam-scanning (radiation pattern). For this purpose, an initial guess (initial phase shifter voltage combination) was generated following the same approach as in the theoretical analysis presented in the previous section but using the experimentally obtained phase curve rather than the calculated one. Once the initial voltage combination is generated, the surface is configured accordingly using the dedicated Arduino-based voltage controller board. After a 5-s pause, the voltage at the second oscilloscope channel is measured. The pause is needed to prevent the measurement from beginning before the RRA is completely reconfigured. Then, the received power is calculated based on the measured voltage value. During the optimization, the transmitting antenna position was kept fixed, and the antenna was oriented so that its boresight would be perpendicular to the RRA to ensure normal wave incidence. The TX antenna was positioned so that its boresight would make with the normal

to the RRA an angle equal to the desired power reflection angle. During the optimization process, both antennas were located at a distance of 1.5 m from the RRA phase shifter layer.

To ensure sufficiently high measurement accuracy and reduce the effect of random fluctuations in the received power level resulting from various interfering signal sources that the receiving antenna can pick up despite being inherently narrowband. The measured data are acquired from the oscilloscope remotely via the VISA interface.

A single voltage combination test cycle involves the following:

- ✓ setting up the required voltages at the DACs outputs,
- ✓ waiting for several seconds to prevent incomplete RRA reconfiguration,
- ✓ receiving power measurement accomplished by the oscilloscope.

With a view to improving the RRA reflective efficiency, a simple random walk optimization was employed to find a phase shifter voltage combination yielding larger levels of the received power than the one obtained by the GO-based phase profile synthesis method. The algorithm proceeds as follows. At each iteration of the random walk algorithm, the voltage combination that has so far demonstrated the largest measured power value (at the very first iteration, the initial guess is used) is used to generate several child combinations (in the present study, the number of child combinations is set to 10) by introducing small changes to each voltage being optimized. To be more specific, a child combination is generated by adding a number drawn from a random number generator to each voltage vector (combination) element. The random number follows a normal distribution with zero mean. To that end, a built-in MATLAB function *randn()* was used. The standard deviation is calculated for each voltage separately according to the difference between adjacent voltage values (except the first and the last ones). Then, for each child combination, the algorithm sends the voltage values to the Arduino-based control board, and following a short pause, the measured received power is retrieved from the oscilloscope.

Sometimes, the optimization algorithm stagnates at a certain voltage combination. This occurs because of sudden and strong background interference level fluctuations, which result in a measured power value larger than those provided by most of the combinations that are close to the previous optimal combination at a time when the fluctuation level is low. Since the voltages tried by the algorithms at the subsequent iterations cannot ensure larger power values, the algorithm sticks to this false optimal combination and cannot escape it. In such cases, one must execute the MATLAB script, implement the algorithm, and return to the voltage combination found before the stagnation.

To be sure that the obtained voltage combination is optimal or close to it, after the optimization, the measurements were made several times with a few minute intervals between the successive measurements. To verify the validity of the obtained results, additional control measurements were made the next day and after a few days to preclude the effect of interference on the voltage combination.

The experimentally obtained radiation patterns are shown in Figures 15 and 16. To highlight the feasibility and justify the utility of the proposed sub-GHz RRA design, the measured radiation patterns acquired for four different RRA configurations, which ensure distinct reflection angles, are accompanied by the radiation pattern measured for a flat metal sheet. The dimensions of the metal sheet are comparable to those of the RRA under study. The pattern measured for the RRA configured to reflect at 30° (see Figure 15a) exhibits the radiation peak occurring exactly at 30° to within the receiver position angle measurement step size of 5 deg. The observed peak is quite sharp, with a maximum reflected power of 2.2 mW. Figure 15b shows the radiation pattern of the RRA with 40°. Each of the patterns was acquired following several measurement-based optimization cycles, each involving 15 iterations with a population size (number of child voltage combinations generated as described above) of 10. The figure reveals that the reflected power peak is at 35°, not 40°. This angle deviation is probably due to the fact that the experimental phase curve was used to generate the initial guess for all four configurations considered. A similar behavior is observed in the case of the 45° configuration—the actual beam steering angle is 40° instead of 45°, as shown in Figure 16a. The worst situation is with the RRA optimization

for 50 degrees. In this case, the maximum occurs at 40° instead of 50° (see Figure 16b), though this configuration ensures higher received power at 50° than the others.

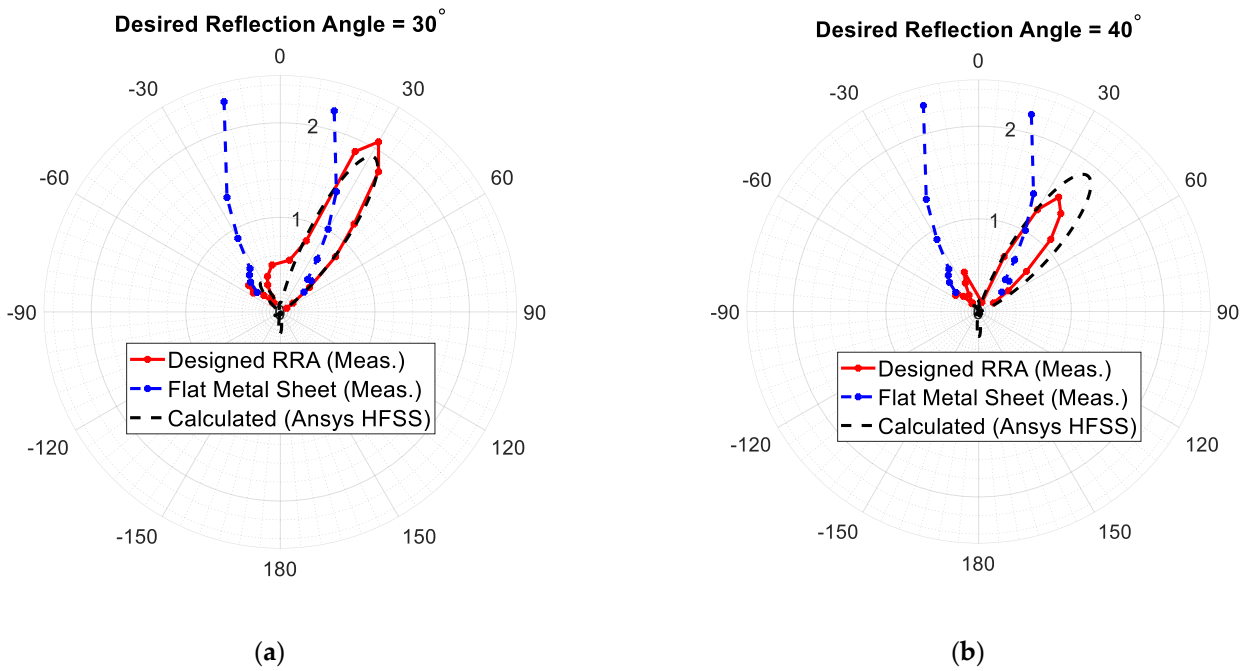


Figure 15. The calculated (red line) and measured (dashed black line) radiation pattern (Rx power in mW) in the azimuthal plane measured for the RRA consisting of 36 (18 × 2) 8-shaped phase shifters (red line) optimized for the desired angle of 30° (a) and 40° (b) and the flat metal sheet used as the reference reflector (blue line).

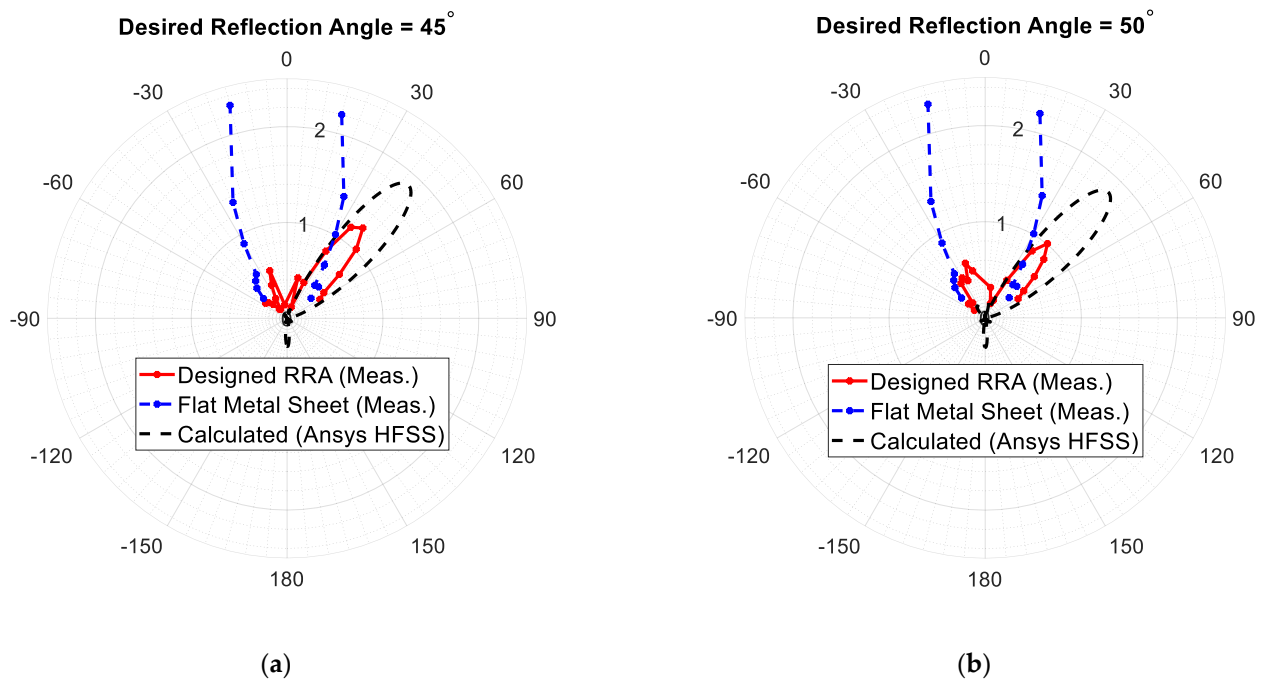


Figure 16. The calculated (red line) and measured (dashed black line) radiation pattern (Rx power in mW) in the azimuthal plane measured for the RRA consisting of 36 (18 × 2) 8-shaped phase shifters (red line) optimized for the desired for the desired angle of 45° (a) and 50° (b) and the flat metal sheet used as the reference reflector (blue line).

Furthermore, in all considered cases, the RRA demonstrated a higher received power level than the flat metal sheet, which confirms the feasibility of the chosen sub-GHz RRA design. It should be mentioned that one could easily achieve more significant amounts of reflected power toward any of the angles examined above compared to those ensured by the RRA just by turning the metal sheet about its vertical axis of symmetry. However, such an approach requires using various electronically controlled motors with sufficiently high durability to maintain uninterrupted operation over a long time period, thus not being sufficiently cost-effective. Moreover, the beam steering speed of such mechanically tunable RRAs is typically substantially lower than that of the varactor-based RRA, thereby limiting the WPT system's adaptability, which is particularly the case with applications involving mobile devices, such as various robotic home appliances.

Once the power is measured for all child combinations, the algorithm takes the voltage combination corresponding to the largest received power value and compares it with the parent combination. If the parent combination gives a power value smaller than the best child combination, the same parent combination is passed to the next iteration; otherwise, the best child is used as the parent combination at the next iteration of the optimization algorithm. The algorithm terminates upon reaching a predefined maximum number of iterations.

5. Conclusions

The paper investigated the possibility of realizing a small footprint reconfigurable reflectarray (RRA) capable of ensuring acceptable power-reflecting efficiency in a sub-GHz band centered at 865.5 MHz. The choice of the configuration was dictated by the fact that it exhibits lower losses and is less expensive than its single-layer counterpart. Additionally, it allows for studying the effect of the thickness on the RRA performance without fabricating multiple prototypes. It was found that increasing the inter-layer separation reduced the reflected wave magnitude variation arising due to various factors, including varactor diode losses; however, it comes at the expense of reduced phase agility. To find a trade-off solution, a numerical model of the unit cell was constructed and analyzed using the commercially available software Ansys HFSS 2023 R1. The examined RRA comprised 36 diode-coupled metallic patches acting as phase shifters.

The numerical results demonstrate that the capacitance range limitation of the currently available varactor diodes results in phase curve broadening, making it tremendously difficult to achieve both high reflection coefficient magnitude uniformity and the full cycle (360°) phase range. Both factors considerably increased the side lobe's level, deteriorating the RRA efficiency, especially at large beam deflection angles. This observation agrees with the findings of other studies on high-frequency RRA designs. However, in the present study, this issue is more pronounced due to the phase curve's inherently lower steepness in the sub-GHz range. For small reflection angles ($<50^\circ$), the classical RRA surface phase profile synthesis approach employing the Generalized Geometrical Optics (GGO) approximation was used. Furthermore, additional numerical studies were carried out to ascertain whether or not it is possible to achieve reasonable high received power in the case of large reflection angles where the conventional GO-based approach fails to ensure adequate efficiency. To that end, the virtual infinite array of supercells was optimized using Ansys HFSS built-in optimization algorithm (Adaptive Multi-Objective (Random Search)). Each cell of the infinite array (supercell) contained an integer number of phase shifters chosen according to the Floquet theory.

For the experimental verification of the developed RRA efficiency, a prototype consisting of 36 phase shifters was fabricated and measured. To compensate for the effect of the varactor diode parameter tolerance on the RRA performance, a random walk-inspired measurement-based optimization was performed in a laboratory. Following the experimental optimization, the received power at several distinct beam-scan angles was measured using two 4-element Yagi antennas. Overall, good agreement between the calculated and measured is observed. The discrepancy in the efficiency at large reflection angles is likely

due to various diode parasitic effects and parameter tolerance that was not fully eliminated by the optimization. Also, a potential source of the discrepancy is the adverse effects of varactor diode biasing network lines that were underestimated in the simulations.

The highest power reflection efficiency was for the RRA configured for the desired reflection angles of 30° . In the case of a 45° RRA configuration, the measured received power was smaller by about a factor of 2, which contrasted with the calculated power. This fact can be explained by higher phase shifter losses than those estimated based on the diode data provided by the manufacturer. To verify this, measured and calculated phase and reflectance magnitude curves were compared at different inter-layer distances (2 cm, 3 cm, and 4 cm). It was found that experimentally obtained curves in all three cases demonstrate higher phase curve slopes and sharper magnitude curve dips, which is indicative of higher losses. The results were compared against a planar metallic reflector under normal illumination. Also, it was demonstrated, albeit only via numerical studies, that using the Floquet mode optimization method, it is possible to design RAs with large beam-scan angles up to 80° .

To summarize, the proposed RRA design has the following advantages, which could make it a promising and attractive means of mitigating the high path-loss issue of adaptable antenna-based WPT systems: passivity (very small amount of power is dissipated by the varactor diodes due to reverse biasing), cost-effectiveness (the phase shifters were printed on a standard FR-4 PCB), manufacturing simplicity (the prototype was fabricated using a simple mechanical milling machine), and compactness. The dimensions along the prototype's azimuth plane are just twice as large as the wavelength at 865.5 MHz. Additionally, the RRA requires no motors to perform beam-steering, allowing for quick adaptability of the underlying antenna-based WPT environment. The results of an in-depth study on the overall performance of WPT systems equipped with such an RRA will be presented in our forthcoming papers.

Author Contributions: Conceptualization, R.K. and A.L.; methodology, R.K. and J.E.; software, R.K., R.B. and K.G.; validation, D.C., K.G. and J.E.; formal analysis, D.C. and R.B.; investigation, R.K., J.E. and D.K.; resources, D.P. and A.L.; data curation, D.C.; writing—original draft preparation, R.K.; writing—review and editing, D.C., J.E. and D.P.; visualization, J.E. and K.G.; supervision, D.P. and A.L.; project administration, D.P.; funding acquisition, D.P. All authors have read and agreed to the published version of the manuscript.

Funding: This research was funded by the Latvian Council of Science, grant No. lzp-2021/1-0170, "Advanced Techniques for Wireless Power Transfer".

Data Availability Statement: Data are contained within the article.

Conflicts of Interest: The authors declare no conflicts of interest.

References

1. Hausteiner, T.; McMenemy, J.; Thiele, L.; Leather, P.S.H. Reconfigurable Intelligent Surface Deployment in 5G and Beyond 5G Cellular Networks. In Proceedings of the 2022 IEEE 23rd International Workshop on Signal Processing Advances in Wireless Communication (SPAWC), Oulu, Finland, 4–6 July 2022; pp. 1–5. [\[CrossRef\]](#)
2. ElMossallamy, M.A.; Zhang, H.; Song, L.; Seddik, K.G.; Han, Z.; Li, G.Y. Reconfigurable Intelligent Surfaces for Wireless Communications: Principles, Challenges, and Opportunities. *IEEE Trans. Cogn. Commun. Netw.* **2020**, *6*, 990–1002. [\[CrossRef\]](#)
3. Chen, Z.; Tang, J.; Zhao, N.; Liu, M.; So, D.K.C. Hybrid Beamforming with Discrete Phase Shifts for RIS-Assisted Multiuser SWIPT System. *IEEE Wirel. Commun. Lett.* **2023**, *12*, 104–108. [\[CrossRef\]](#)
4. Ren, H.; Chen, Z.; Hu, G.; Peng, Z.; Pan, C.; Wang, J. Transmission Design for Active RIS-Aided Simultaneous Wireless Information and Power Transfer. *IEEE Wirel. Commun. Lett.* **2023**, *12*, 600–604. [\[CrossRef\]](#)
5. Berry, D.; Malech, R.; Kennedy, W. The Reflectarray Antenna. *IEEE Trans. Antennas Propag.* **1963**, *11*, 645–651. [\[CrossRef\]](#)
6. Hum, S.V.; Perruisseau-Carrier, J. Reconfigurable Reflectarrays and Array Lenses for Dynamic Antenna Beam Control: A Review. *IEEE Trans. Antennas Propag.* **2014**, *62*, 183–198. [\[CrossRef\]](#)
7. Pozar, D.M.; Metzler, T.A. Analysis of a RA Antenna Using Microstrip Patches of Variable Size. *Electron. Lett.* **1993**, *29*, 657. [\[CrossRef\]](#)
8. Pozar, D.M.; Targonski, S.D.; Syrigos, H.D. Design of Millimeter Wave Microstrip Reflectarrays. *IEEE Trans. Antennas Propag.* **1997**, *45*, 287–296. [\[CrossRef\]](#)

9. Bialkowski, M.E.; Sayidmarie, K.H. Investigations into Phase Characteristics of a Single-Layer RA Employing Patch or Ring Elements of Variable Size. *IEEE Trans. Antennas Propag.* **2008**, *56*, 3366–3372. [[CrossRef](#)]
10. Huang, J. Microstrip Reflectarray. In Proceedings of the Antennas and Propagation Society Symposium 1991 Digest, London, ON, Canada, 24–28 June 1991; pp. 612–615. [[CrossRef](#)]
11. Huang, J.; Encinar, J.A. *Reflectarray Antennas*; IEEE Press: Piscataway, NJ, USA; Hoboken, NJ, USA; Wiley-Interscience: New York, NY, USA, 2008.
12. Zhang, G.; Lu, Y.; Lin, Y.; Zhong, Z.; Ding, Z.; Niyato, D. AoI Minimization in RIS-Aided SWIPT Systems. *IEEE Trans. Veh. Technol.* **2024**, *73*, 2895–2900. [[CrossRef](#)]
13. Zhao, M.M.; Xu, K.; Cai, Y.; Niu, Y.; Hanzo, L. Secrecy Rate Maximization of RIS-Assisted SWIPT Systems: A Two-Timescale Beamforming Design Approach. *IEEE Trans. Wirel. Commun.* **2023**, *22*, 4489–4504. [[CrossRef](#)]
14. Mei, P.; Zhang, S.; Pedersen, G.F. A Low-Cost, High-Efficiency and Full-Metal Reflectarray Antenna with Mechanically 2-D Beam-Steerable Capabilities for 5G Applications. *IEEE Trans. Antennas Propag.* **2020**, *68*, 6997–7006. [[CrossRef](#)]
15. Boccia, L.; Amendola, G.; Di Massa, G. A Microstrip Patch Antenna Oscillator for Reflectarray Applications. In Proceedings of the IEEE Antennas and Propagation Society Symposium, Monterey, CA, USA, 20–25 June 2004; pp. 3927–3930.
16. Boccia, L.; Venneri, F.; Amendola, G.; Di Massa, G. Application of Varactor Diodes for Reflectarray Phase Control. In Proceedings of the IEEE Antennas and Propagation Society International Symposium (IEEE Cat. No.02CH37313), San Antonio, TX, USA, 16–21 June 2002. [[CrossRef](#)]
17. Riel, M.; Laurin, J.J. Design of an Electronically Beam Scanning Reflectarray Using Aperture-Coupled Elements. *IEEE Trans. Antennas Propag.* **2007**, *55*, 1260–1266. [[CrossRef](#)]
18. Perez-Palomino, G.; Baine, P.; Dickie, R.; Bain, M.; Encinar, J.A.; Cahill, R.; Barba, M.; Toso, G. Design and Experimental Validation of Liquid Crystal-Based Reconfigurable Reflectarray Elements with Improved Bandwidth in F-Band. *IEEE Trans. Antennas Propag.* **2013**, *61*, 1704–1713. [[CrossRef](#)]
19. Qureshi, S.A.; Kamarudin, M.R.; Abbasi, M.I.; Abidin, Z.Z.; Dahri, M.H. VO-2 Assisted Unit Cell for Designing THz Reconfigurable RA Antenna. In Proceedings of the 2023 IEEE International Symposium on Antennas and Propagation (ISAP), Kuala Lumpur, Malaysia, 30 October–2 November 2023; pp. 1–2. [[CrossRef](#)]
20. Ramsey, J.; Henderson, K.; Ghalichechian, N. Thermally Actuated Vanadium Dioxide Millimeter Wave Reflectarray. In Proceedings of the 2022 16th European Conference on Antennas and Propagation (EuCAP), Madrid, Spain, 27 March–1 April 2022; pp. 1–3. [[CrossRef](#)]
21. Romanofsky, R.R. Advances in Scanning Reflectarray Antennas Based on Ferroelectric Thin-Film Phase Shifters for Deep-Space Communications. *Proc. IEEE* **2007**, *95*, 1968–1975. [[CrossRef](#)]
22. Webb, G.W.; Angello, S.; Vernon, W.; Sanchez, M.S.; Rose, S.C. Novel Photonically Controlled Antenna for MMW Communications. In Proceedings of the International Topical Meeting on Microwave Photonics MWP 2000 (Cat. No.00EX430), Oxford, UK, 11–13 September 2000; pp. 97–100. [[CrossRef](#)]
23. Carrasco, E.; Perruisseau-Carrier, J. Reflectarray Antenna at Terahertz Using Graphene. *IEEE Antennas Wirel. Propag. Lett.* **2013**, *12*, 253–256. [[CrossRef](#)]
24. Bayraktar, O.; Civi, O.A.; Akin, T. Beam Switching Reflectarray Monolithically Integrated with RF MEMS Switches. *IEEE Trans. Antennas Propag.* **2012**, *60*, 854–862. [[CrossRef](#)]
25. Legay, H.; Pinte, B.; Charrier, M.; Ziaei, A.; Girard, E.; Gillard, R.A. Steerable Reflectarray Antenna with Mems Controls. In Proceedings of the IEEE International Symposium on Phased Array Systems and Technology, Boston, MA, USA, 14–17 October 2003; pp. 494–499. [[CrossRef](#)]
26. Ren, J.; Menzel, W. Dual-Frequency Folded Reflectarray Antenna. *IEEE Antennas Wirel. Propag. Lett.* **2013**, *12*, 1216–1219. [[CrossRef](#)]
27. Huang, J. Bandwidth Study of Microstrip Reflectarray and a Novel Phased Reflectarray Concept. In Proceedings of the IEEE Antennas and Propagation Society International Symposium, Newport Beach, CA, USA, 18–23 June 1995; pp. 582–585.
28. Encinar, J.A.; Zornoza, J.A. Broadband Design of Three-Layer Printed Reflectarrays. *IEEE Trans. Antennas Propag.* **2003**, *51*, 1662–1664. [[CrossRef](#)]
29. Carrasco, E.; Encinar, J.A.; Barba, M. Bandwidth Improvement in Large Reflectarrays by Using True-Time Delay. *IEEE Trans. Antennas Propag.* **2008**, *56*, 2496–2503. [[CrossRef](#)]
30. Nayeri, P.; Yang, F.; Elsherbeni, A.Z. Broadband Reflectarray Antennas Using Double-Layer Subwavelength Patch Elements. *IEEE Antennas Wirel. Propag. Lett.* **2010**, *9*, 1139–1142. [[CrossRef](#)]
31. Edalati, A.; Sarabandi, K. Wideband Reflectarray Antenna Based on Miniaturized Element Frequency Selective Surfaces. In Proceedings of the 2012 6th European Conference on Antennas and Propagation (EUCAP), Prague, Czech Republic, 26–30 March 2012; pp. 362–364. [[CrossRef](#)]
32. Qin, P.Y.; Guo, Y.J.; Weily, A.R. Broadband Reflectarray Antenna Using Subwavelength Elements Based on Double Square Meander-Line Rings. *IEEE Trans. Antennas Propag.* **2016**, *64*, 378–383. [[CrossRef](#)]
33. Zhu, J.; Yang, Y.; Liao, S.; Xue, Q. Additively Manufactured Metal-Only Waveguide-Based Millimeter-Wave Broadband Achromatic RAs. *IEEE Trans. Antennas Propag.* **2023**, *71*, 6185–6190. [[CrossRef](#)]
34. Liu, C.; Hum, S.V. Electronically Tunable Single-Layer Reflectarray Antenna Element with Improved Bandwidth. *IEEE Antennas Wirel. Propag. Lett.* **2010**, *9*, 1241–1244. [[CrossRef](#)]

35. Awan, W.A.; Hussain, N.; Park, S.G.; Kim, N. Programmable Metasurface-Based Wideband Antenna for High-Gain Beam-Steering and Pattern-Reconfigurability Applications. In Proceedings of the 2023 XXXVth General Assembly and Scientific Symposium of the International Union of Radio Science (URSI GASS), Sapporo, Japan, 19–26 August 2023; pp. 1–4.
36. Sangmahamad, P.; Janpugdee, P.; Zhao, Y.A. Metasurface-Based Electronically Reconfigurable and Dual-Polarized Reflectarray Antenna for Beam-Steering Applications. *IEEE Access* **2023**, *11*, 137414–137425. [[CrossRef](#)]
37. Xu, L.; Ge, X.; Zhang, Q.; Dang, F.; Zhang, P.; Liu, J.; Yuan, C. A Beam-Steerable Wideband Reflectarray Antenna for C-Band High-Power Microwave Application. *IEEE Access* **2023**, *11*, 64559–64566. [[CrossRef](#)]
38. Xu, L.; Yuan, C.; Zhang, Q.; Liu, J.; Zhang, Q.; Sun, Y. Design and Experiments of a Beam-Steerable Wideband Reflectarray Antenna for High-Power Microwave Applications. *IEEE Trans. Antennas Propag.* **2023**, *71*, 1955–1959. [[CrossRef](#)]
39. Li, W.; Gao, S.; Zhang, L.; Luo, Q.; Cai, Y. An Ultra-Wide-Band Tightly Coupled Dipole Reflectarray Antenna. *IEEE Trans. Antennas Propag.* **2018**, *66*, 533–540. [[CrossRef](#)]
40. Han, J.; Li, L.; Liu, G.; Wu, Z.; Shi, Y.A. Wideband 1 Bit 12×12 Reconfigurable Beam-Scanning Reflectarray: Design, Fabrication, and Measurement. *IEEE Antennas Wirel. Propag. Lett.* **2019**, *18*, 1268–1272. [[CrossRef](#)]
41. Yu, A.; Yang, F.; Elsherbeni, A.Z.; Huang, J. Experimental Demonstration of a Single Layer Tri-Band Circularly Polarized RA. In Proceedings of the 2010 IEEE Antennas and Propagation Society International Symposium, Toronto, ON, Canada, 11–17 July 2010; pp. 1–4. [[CrossRef](#)]
42. Smith, T.; Gothelf, U.; Kim, O.S.; Breinbjerg, O. An FSS-Backed 20/30 GHz Circularly Polarized Reflectarray for a Shared Aperture L- and Ka-Band Satellite Communication Antenna. *IEEE Trans. Antennas Propag.* **2014**, *62*, 661–668. [[CrossRef](#)]
43. Ahmadi, F.; Forooraghi, K.; Atlasbaf, Z.; Virdee, B. Dual Linear-Polarized Dielectric Resonator Reflectarray Antenna. *IEEE Antennas Wirel. Propag. Lett.* **2013**, *12*, 635–638. [[CrossRef](#)]
44. Hashiguchi, H.; Michishita, N.; Morishita, H.; Matsuno, H.; Ohto, T.; Nakano, M. Reduction of Sidelobe Level for Dual Frequency and Dual Polarization Reflectarray. In Proceedings of the 2022 16th European Conference on Antennas and Propagation (EuCAP), Madrid, Spain, 27 March–1 April 2022; pp. 1–5. [[CrossRef](#)]
45. Zhou, S.G.; Huang, G.L.; Chio, T.H. A Lightweight, Wideband, Dual-Circular-Polarized Waveguide Cavity Array Designed with Direct Metal Laser Sintering Considerations. *IEEE Trans. Antennas Propag.* **2018**, *66*, 675–682. [[CrossRef](#)]
46. Florencio, R.; Encinar, J.A.; Boix, R.R.; Barba, M.; Toso, G. Flat Reflectarray that Generates Adjacent Beams by Discriminating in Dual Circular Polarization. *IEEE Trans. Antennas Propag.* **2019**, *67*, 3733–3742. [[CrossRef](#)]
47. Zhang, M.T.; Gao, S.; Jiao, Y.C.; Wan, J.X.; Tian, B.N.; Wu, C.B.; Farrall, A.J. Design of Novel Reconfigurable Reflectarrays with Single-Bit Phase Resolution for Ku-Band Satellite Antenna Applications. *IEEE Trans. Antennas Propag.* **2016**, *64*, 1634–1641. [[CrossRef](#)]
48. Yang, H.; Yang, F.; Xu, S.; Mao, Y.; Li, M.; Cao, X.; Gao, J. A 1-Bit 10×10 Reconfigurable RA Antenna: Design, Optimization, and Experiment. *IEEE Trans. Antennas Propag.* **2016**, *64*, 2246–2254. [[CrossRef](#)]
49. Wang, Z.X.; Cheng, Q.; Cui, T.J. A 1-Bit Dual Linearly Polarized Reconfigurable Reflectarray Element in X-Band. In Proceedings of the 2023 IEEE MTT-S International Wireless Symposium (IWS), Qingdao, China, 14–17 May 2023; pp. 1–3.
50. Hu, J.; Chi, P.L.; Yang, T. Novel 1-Bit Beam-Scanning Reflectarray with Switchable Linear, Left-Handed, or Right-Handed Circular Polarization. *IEEE Trans. Antennas Propag.* **2023**, *71*, 1548–1556. [[CrossRef](#)]
51. Pan, L.; Li, K.; Li, N.; Cai, Y. A Dual-Polarized Electronically Scanned Reflectarray Based on 2-Bit Reconfigurable Element. In Proceedings of the 2023 16th UK-Europe-China Workshop on Millimetre Waves and Terahertz Technologies (UCMMT), Guangzhou, China, 31 August–3 September 2023; pp. 1–3. [[CrossRef](#)]
52. Shabanpour, J.; Simovski, C.R. Angular and Polarization Stability of Broadband Reconfigurable Intelligent Surfaces of Binary Type. *IEEE Access* **2022**, *10*, 126253–126268. [[CrossRef](#)]
53. Yin, J.; Li, Y.; Zwick, T. A Miniaturized 1-Bit Reflective Unit Cell for Reconfigurable Intelligent Surface. In Proceedings of the 2023 53rd European Microwave Conference (EuMC), Berlin, Germany, 19–21 September 2023; pp. 528–531.
54. Xue, H.; Lu, Z.; Ma, X.; Wang, Z.; Zhu, L.; Yue, S.; Han, J.; Liu, H.; Li, L. A Reconfigurable Metasurface Enhancing Signal Coverage for Wireless Communication Using Reduced Numbers of PIN Diodes. *IEEE Trans. Microw. Theory Tech.* **2024**, *72*, 1964–1978. [[CrossRef](#)]
55. Kashyap, B.G.; Theofanopoulos, P.C.; Cui, Y.; Trichopoulos, G.C. Fabrication and Characterization of a 900-Element 222. In 5 GHz Single-Bit Reflective Surface with Suppressed Quantization Lobes. In Proceedings of the 2021 United States National Committee of URSI National Radio Science Meeting (USNC-URSI NRSM), Boulder, CO, USA, 4–9 January 2021; pp. 153–154.
56. Omoto, K.; Tomura, T.; Sakamoto, H.; Hirokawa, J.; Okuma, M. Basic Study on Deformation Reconfiguration Technology for 5. In 8-GHz-Band Reflectarray Antennas. In Proceedings of the 2019 Photonics & Electromagnetics Research Symposium—Fall (PIERS—Fall), Xiamen, China, 17–20 December 2019; pp. 290–294. [[CrossRef](#)]
57. Omoto, K.; Tomura, T.; Sakamoto, H. Proof-of-Concept on Misalignment Compensation for 5.8-GHz-Band Reflectarray Antennas by Varactor Diodes. *IEEE Access* **2021**, *9*, 54101–54108. [[CrossRef](#)]
58. Jiang, H.; Dou, W. Optimal Design of Microstrip Reflectarray Antenna to Maximize Transmission Distance for Microwave Wireless Power Transmission. In Proceedings of the 2021 15th European Conference on Antennas and Propagation (EuCAP), Düsseldorf, Germany, 22–26 March 2021; pp. 1–4.
59. Yu, S.; Liu, H.; Li, L. Design of Near-Field Focused Metasurface for High-Efficient Wireless Power Transfer with Multifocus Characteristics. *IEEE Trans. Ind. Electron.* **2019**, *66*, 3993–4002. [[CrossRef](#)]

60. Yu, N.; Genevet, P.; Kats, M.A.; Aieta, F.; Tétienne, J.P.; Capasso, F.; Gaburro, Z. Light Propagation with Phase Discontinuities: Generalized Laws of Reflection and Refraction. *Science* **2011**, *334*, 333–337. [[CrossRef](#)]
61. Vassos, E.; Churm, J.; Feresidis, A. Design Process of Novel Electro-Mechanically Tuneable Reflectarray Antennas. In Proceedings of the 2021 51st European Microwave Conference (EuMC), London, UK, 4–6 April 2022; pp. 155–157.
62. Makdissy, T.; Hassoun, I. Coupled Slots Varactor-Tuned Unit Cell for Single Linear Polarization Reflectarrays at C-Band. In Proceedings of the 2020 IEEE International RF and Microwave Conference (RFM), Kuala Lumpur, Malaysia, 14–16 December 2020; pp. 1–4.
63. Díaz-Rubio, A.; Asadchy, V.S.; Elsakka, A.; Tretyakov, S.A. From the Generalized Reflection Law to the Realization of Perfect Anomalous Reflectors. *Sci. Adv.* **2017**, *3*, e1602714. [[CrossRef](#)] [[PubMed](#)]
64. Asadchy, V.S.; Albooyeh, M.; Tcvetkova, S.N.; Díaz-Rubio, A.; Ra’di, Y.; Tretyakov, S.A. Perfect Control of Reflection and Refraction Using Spatially Dispersive Metasurfaces. *Phys. Rev. B* **2016**, *94*, 075142. [[CrossRef](#)]
65. Brillouin, L. *Wave Propagation in Periodic Structures; Electric Filters and Crystal Lattices*; Dover Publications: New York, NY, USA, 1953.
66. Ansys HFSS | 3D High Frequency Simulation Software. Available online: <https://www.ansys.com/products/electronics/ansys-hfss> (accessed on 21 September 2021).
67. Skyworks Solutions. SMV1763 Series: Hyperabrupt Junction Tuning Varactors. *Datasheet*. 2015, pp. 1–9. Available online: https://www.skyworksinc.com/-/media/SkyWorks/Documents/Products/101-200/SMV1763_Series_200072M.pdf (accessed on 14 April 2024).
68. Ozdogan, O.; Bjornson, E.; Larsson, E.G. Intelligent Reflecting Surfaces: Physics, Propagation, and Pathloss Modeling. *IEEE Wirel. Commun. Lett.* **2020**, *9*, 581–585. [[CrossRef](#)]
69. Balanis, C.A. *Advanced Engineering Electromagnetics*; J. Wiley & Sons: Hoboken, NJ, USA, 2012.
70. Budhu, J.; Grbic, A. Perfectly Reflecting Metasurface Reflectarrays: Mutual Coupling Modeling Between Unique Elements through Homogenization. *IEEE Trans. Antennas Propag.* **2021**, *69*, 122–134. [[CrossRef](#)]
71. Movahediqomi, M.; Ptitsyn, G.; Tretyakov, S.A. Comparison between Different Designs and Realizations of Anomalous Reflectors for Extreme Deflections. *IEEE Trans. Antennas Propag.* **2023**, *71*, 8007–8017. [[CrossRef](#)]
72. Kosulnikov, S.; Wang, X.; Tretyakov, S.A. Discrete-Impedance Metasurfaces for Wireless Communications in D-Band. *IEEE Trans. Antennas Propag.* **2024**, *72*, 591–599. [[CrossRef](#)]
73. Epstein, A.; Eleftheriades, G.V. Synthesis of Passive Lossless Metasurfaces Using Auxiliary Fields for Reflectionless Beam Splitting and Perfect Reflection. *Phys. Rev. Lett.* **2016**, *117*, 256103. [[CrossRef](#)]
74. Epstein, A.; Eleftheriades, G.V. Arbitrary Power-Conserving Field Transformations with Passive Lossless Omega-Type Bianisotropic Metasurfaces. *IEEE Trans. Antennas Propag.* **2016**, *64*, 3880–3895. [[CrossRef](#)]

Disclaimer/Publisher’s Note: The statements, opinions and data contained in all publications are solely those of the individual author(s) and contributor(s) and not of MDPI and/or the editor(s). MDPI and/or the editor(s) disclaim responsibility for any injury to people or property resulting from any ideas, methods, instructions or products referred to in the content.